Velocity Measurements and Flow Visualization in Low Viscosity Jets

A THESIS
SUBMITTED TO THE FACULTY OF THE GRADUATE SCHOOL
OF THE UNIVERSITY OF MINNESOTA
BY

Ian Stanley Wright

IN PARTIAL FULFILLMENT OF THE REQUIREMENTS
FOR THE DEGREE OF
MASTER OF SCIENCE

Vinod Srinivasan

August, 2020

Acknowledgements

This work involved the input and contributions of many people. I would first like to give my appreciation to my advisor, Dr. Vinod Srinivasan, for his help and guidance. Special thanks goes to the senior members of our lab, Manish Sachdeva, Ankit Saini, and Sankar Muthukrishnan for their lessons, insight, and encouragement. Further credit is due to undergraduate researchers Joe Kuntz and Peter Rohrbach, for their contributions to data collection and fabrication of the experimental facility. Finally, my sincerest thanks to Zak Kujala for the uncountable hours spent learning and investigating the field of fluid dynamics together.

Abstract

Mixing of a liquid jet into a surrounding fluid is a commonly encountered phenomenon in both natural and engineering systems. Understanding the influence of viscosity ratio on jet stability can help design fluid systems with enhanced or suppressed mixing characteristics. Experiments were conducted with low viscosity axisymmetric liquid jets to characterize the behavior of instabilities as a function of viscosity ratio. In the experiment, viscosity ratios M (ambient-to-jet) from 1 to 50 were imaged in a constant density environment at jet Reynolds numbers ranging from 794 to 2464. Images display a change from axisymmetric jet breakup to a helical mode at high Reynolds numbers and high ambient-to-jet viscosity ratios. Additionally, hot film velocity measurements were taken to characterize the jet profile and quantitatively measure both the mean and fluctuating velocity fields. The spectral data captured singular peaks in the frequency domain, in the range of 6-30 Hz. This peak frequency was further shown to have a dependence on both the jet Reynolds number and the ambient-to-jet viscosity ratio. Images of jet breakup, jet velocity profiles, and velocity instability spectra are shown and discussed.

Contents

List of Figures

Chapter 1

Introduction

The present work examines the breakdown of an axisymmetric circular free jet under the influence of an ambient-to-jet viscosity ratio. For this experimental investigation, a novel facility is fabricated, consisting of a large quiescent tank into which flows a smooth laminar jet. The overall goal is to demonstrate that the facility and measurement system can generate a viscosity stratified jet and record its behavior, and then to document the observed stability attributes of the system for later comparison to stability theory.

Experimental stability studies have been an important part of fluid dynamics for over a century. In 1923, Taylor famously predicted and then experimentally observed the onset of Taylor vortices in Couette flow. Since then, a large number of stability studies have been performed, reaching into nearly every area of fluid dynamics from aeronautics to geodynamics. Even with all of the disparate applications, at the core there are a number of well-documented canonical flows that serve as a basis for applied problem solving. For example, the simplified study of two parallel horizontal streams of different velocity - Kelvin-Helmholtz instability - has explained observations in cloud formations (Drazin and Reid 1981) and oceanic flow (Woods, 1969). Confined flows such as Taylor-Couette flow and strictly parallel flows such as Kelvin-Helmholtz flow form the foundation of stability theory and introduce widely usable concepts. Many shear flows of interest, however, are of unbounded nature with some evolution in space. These shear flows include often encountered flows such as mixing layers, boundary layers, wakes, and jets. As explained in the following section, much of the foundational theory from basic flows can be leveraged for use in open and quasi-parallel flows. The studies of these open

ows is of particular interest, due to their relevance in natural and engineering systems. As reviewed in the next section, a number of clever studies have well documented the instabilities present in these open ows, yielding important insight for designers seeking to control ow systems. The present undertaking is motivated by the desire to add to this base of knowledge, by including the heretofore neglected in uence of viscosity variation in open ows through the study of variable viscosity jet ow stability.

Examples of ows with viscosity strati cation abound, existing nearly any time that a composition or temperature di erence is present across a ow. The range of viscosity di erence depends on the system, but cases with signi cant variation are commonly found. Examples in nature include glacier, magma, and saltwater - freshwater ows. As for engineering systems, the chemical and food processing industries include countless cases of mixing uids of dissimilar viscosities. Another engineering example is the plasma industry, where in plasma spray torches a jet is surrounded by a gas of vastly di erent viscosity. Wastewater management and industrial cooling systems also exhibit viscosity variation, where a uid is discharged into a large body of another uid of dissimilar viscosity. In these industry examples, rapid and e cient mixing is often desired to save time, money, and - in the case of the wastewater systems - to decrease environmental impact. Understanding the stability characteristics of ows with viscosity variation will enable more accurate modeling of natural ows, and help with the design of engineering systems with enhanced mixing characteristics.

This thesis begins with a theoretical background introducing stability concepts and explaining the relevance of viscosity variation to such concepts. Following this theory is a review of important experimental work related to the documentation of hydrodynamic stability in open ows. Next, the motivation and goals are stated, before moving on to describe the new experimental apparatus constructed for this study and the technique of experimentation in such an apparatus. The results are then presented with analysis, before a discussion is given and the thesis concluded.

Chapter 2

Background

Linear stability theory forms the basis of the theoretical background to the present study. This work, however, is truly experimental in nature, and so stability theory is presented in this section not as a full account, but instead in such a way to motivate the experimental work and provide a framework for which to understand the experimental design and decisions made. Attempts have been made to keep the explanations intuitive, so that the reader may better understand the reasoning behind the work. In this section, a theoretical introduction is first given to basic stability concepts. Next, the stability concepts are applied further to flows with viscous stratification, showing that such stratification can be influential. Following the theory is a summary of the important prior experimental work relevant to the current study.

2.1 Theoretical Background

2.1.1 Stability Concept Overview

The concept of hydrodynamic stability may be best introduced by an illustration of mechanical stability. Figure 2.1 shows a ball in three separate scenarios. A finite impulse force is imagined to be applied to the ball, and the response of the ball is monitored over time. If the ball returns to its original position, it is considered stable. If instead the ball does not return, it is unstable. Other, nonlinear configurations can be imagined where only impulses of a certain magnitude result in a permanent change

in the ball location.

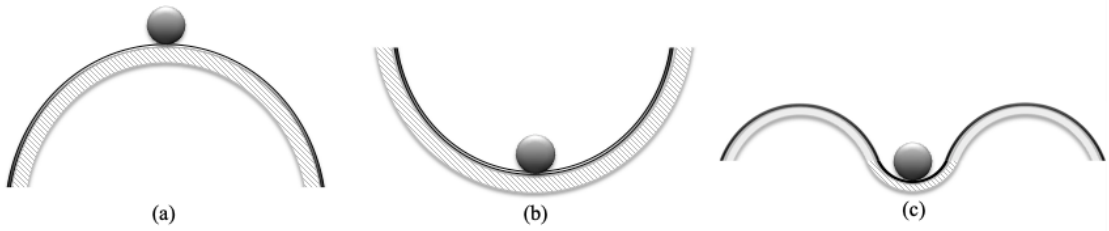

Figure 2.1: Illustration of stability in a mechanical sense. Figure (a) shows an unstable con guration, where any force on the ball will result in the ball being permanently removed from its present state. Figure (b) shows a stable con guration, as any movement of the ball will be damped, and it will soon return to the same position. Figure (c) is nonlinearly unstable, where a small force may be damped out, but a large enough force will result in the ball moving from its position.

The uid dynamics, the study of stability concerns itself with the response of a laminar ow to some small amplitude ow disturbance. If the ow returns to its original laminar state, the ow is considered stable. If instead the disturbance grows so that the base laminar ow becomes altered, it is considered unstable.

Mathematically, this concept is facilitated by beginning with a base ow and superimposing an in nitesimal sinusoidal disturbance, here explained following the normal mode method referenced from Kundu (2015). For example, consider a parallel ow along the x-axis with variation in the y-direction:

$$\boldsymbol{U} = U(y)\hat{\boldsymbol{e}}_x \tag{2.1}$$

Upon this base ow is superimposed a disturbance of form:

$$u(x, y, z, t) = \hat{u}(y)e^{i(\alpha x + \beta z) + \sigma t} \tag{2.2}$$

where $\hat{u}(y)$ is a complex amplitude, i is the imaginary number $\sqrt{-1}$, where α and β denote the streamwise and spanwise wave numbers, respectively, and σ is the temporal growth rate with both real and imaginary components $\sigma = \sigma_r + i\sigma_i$.

The flow is then analyzed with respect to all possible wavenumbers, and the positive or negative growth rate tells the stability:

$$\sigma_r < 0 \text{ is a stable flow}$$
$$\sigma_r = 0 \text{ is a marginally stable flow}$$
$$\sigma_r > 0 \text{ is an unstable flow}$$

It is important to reiterate that if σ_r is positive for *any* wavenumber, the flow is considered unstable.

Unstable flows are furthermore divided into two classifications: convectively and absolutely unstable. This distinction, first fully explained by plasma physicists Twiss (1951) and Landau & Lifshitz (1959), is illustrated by Figure 2.2. In convective instability, a disturbance grows as it travels downstream. Any single location downstream of the impulse will experience the disturbance, but given a long enough time, the disturbance will pass and the single location will return to its base state. This can be seen in Figure 2.2(a), by following a vertical line up through any point on the positive x-axis. This line corresponds to passing time. The line will intersect the disturbance, but will once again exit the disturbance wedge when sufficient time has passed. Convectively unstable flows can be thought of as amplifiers, which will spatially amplify any small disturbance down the flow. As such, the state of the flow at any given position is dependent on the amplitude and location of the original disturbance. Absolute instability, however, differs in that the disturbance propagates upstream as well as downstream in the flow. This can be seen in Figure 2.2(b), where the disturbance wedge now extends up and out from both sides of the origin. This wedge includes the line above the origin, showing that there is some amplified disturbance that has a group velocity of zero. Because the disturbance now travels in both directions, the original impulse, no matter how small, will grow to consume the entire flow field. This is seen in Figure 2.2 again following a vertical line from any x location in (b), and seeing that the line enters the unstable wedge and never leaves. This means that for absolutely unstable flows, in time an initial disturbance will permanently alter the base flow everywhere. As such, the future state of an absolutely unstable flow, unlike convectively unstable flows, does not depend on the location or magnitude of the original disturbance. Because of this behavior, absolutely unstable flows are called self-excited, as once some small disturbance is introduced, no additional input is needed to sustain the response.

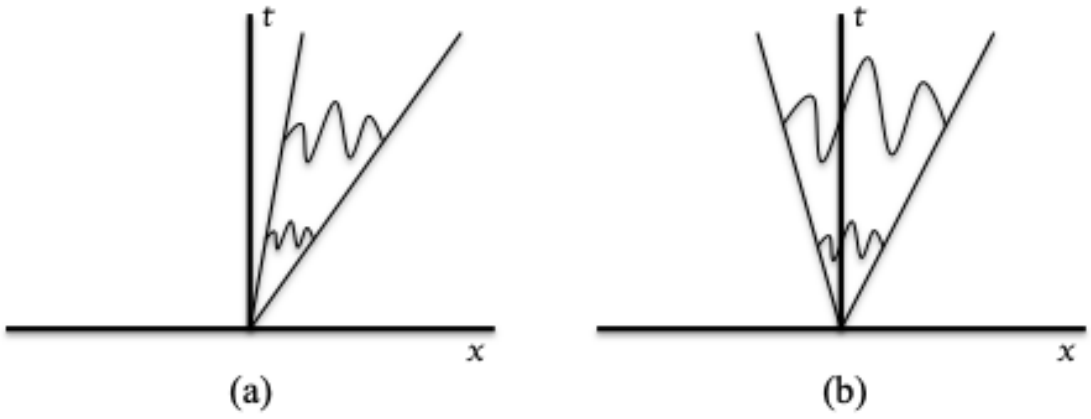

Figure 2.2: Diagram of the convective and absolute instability response to a single traveling wave ow disturbance. Convective instability (a) is shown next to absolute instability (b). Disturbances within the wedge are ampli ed ($\sigma > 0$) while all outside disturbances are damped ($\sigma < 0$).

It should be noted that linear stability theory disregards the highly nonlinear behavior present in many real ows. However, linear stability theory remains useful in that it predicts the initial growth of disturbances. In unstable ow conditions where disturbances are highly ampli ed, the in nitesimal disturbance wave that grows rst will likely later dominate the ow. For this reason, linear stability theory has enjoyed success even when applied to nonlinear applications, because it still accurately predicts useful information such as the frequency of the dominant unstable mode.

Linear stability analysis includes the additional simpli cation of assuming that the base ow pro le does not change in the streamwise direction. Most engineering or laboratory ows, however, are not parallel and exhibit some change in the velocity pro le as the ow develops downstream. Such realistic ows are called spatially developing ows, and include such commonly encountered ows such as mixing layers, jets, wakes, and boundary layers. Yet, even though the velocity pro les change downstream, the pro le over some small portion of the ow { such as in the initial region of a jet { is generally su ciently parallel to be modeled as such. More precisely, if the wavelength of the disturbance is small as compared to the spatial variation in the ow, than the parallel assumption can be used (Huerre and Monkewitz, 1990). In this way, linear stability theory works to predict the onset of nonlinearity, but is not applicable thereafter.

The method of splitting spatially developing ows into quasi-parallel subregions necessitates the introduction of the terms \local" and \global". A local instability refers to an instability determined from the velocity pro le present at a single downstream location. This single velocity pro le, when analyzed, can be either convectively or absolutely unstable. Therefore, the stability of this single downstream location is described as "locally convectively unstable" or "locally absolutely unstable". In contrast, global instability refers to the stability of the entire ow eld. The global stability of a ow is in uenced by the local stability characteristics of the included local velocity pro les.

Flows transition from convective to absolute instability with changes in velocity pro le, or other characteristics including surface tension, density, and viscosity. And with global instabilities come dramatic changes in behavior over the entire ow eld. Therefore, a major focus of hydrodynamic stability is predicting and measuring the characteristics of ows which are globally unstable, and determining the controlling parameters that make it so.

2.1.2 Stability with Viscosity Stratification

To illustrate the importance of viscous strati cation on stability, the linear stability governing equations are presented here for a basic unidirectional ow. This method presupposes knowledge of some stability theory concepts, and the reader should refer to Schmid and Henningson (2000) for a full background in the analysis. A ow is considered in three dimensions with viscosity gradients in the method of Sahu & Matar (2010). Here, the base and uctuating quantities are given in the method described previously in equations 2.1 and 2.2 (ex: $U = U(y) + u(x, y, z, t)$). As such, the perturbation equations for ow-normal direction velocity, vorticity, or viscosity are given, as in Govindarajan (2014), by:

$$(\hat{v}, \hat{\eta}, \hat{\mu}) = (v(y), \eta(y), \mu(y))e^{[i(\alpha x + \beta z \quad \omega t)]} \tag{2.3}$$

In equation 2.3, α and β are the wavenumbers in the streamwise and spanwise directions, ω is the frequency, and $c = \omega/\alpha$ is the phase speed of the disturbance mode. When the imaginary part of the frequency is greater than zero, $\omega_i > 0$, the ow is unstable.

The Reynolds number for the ow is then de ned as:

$$Re \quad \frac{U_{\text{ref}} H \rho}{\mu_{\text{ref}}} \tag{2.4}$$

where the reference values are typically taken from the maximum values in the ow. The density is ρ and a typical length scale H is chosen in the direction of variation: the y direction in this example. The base ow viscosity $\mu(y)$ is nondimensionalized by scaling with the reference viscosity μ_{ref}. Viscosity is generally a function of another quantity, such as temperature or concentration.

The ow quantities are substituted into the linearized Navier Stokes equations, and are then expressed in normal mode form as:

$$\begin{aligned}[v'' \quad (\alpha^2 + \beta^2)v](U \quad c) \quad U''v = \frac{1}{i\alpha Re}[\mu[v'''' \quad 2(\alpha^2 + \beta^2)v'' + (\alpha^2 + \beta^2)^2 v] \\ + 2\mu'[v'''' \quad (\alpha^2 + \beta^2)v'] + \mu''[v'' + (\alpha^2 + \beta^2)v] \\ i\alpha U'[\mu'' + \mu(\alpha^2 + \beta^2)] \quad 2i\alpha U''\mu' \quad i\alpha U'''\mu]\end{aligned} \tag{2.5}$$

$$\eta(U \quad c) + \frac{\beta}{\alpha} U'\eta = \frac{1}{i\alpha Re}[\mu[\eta'' \quad (\alpha^2 + \beta^2)\eta] + \mu'\eta' + i\beta U'\mu' + i\beta U''\mu] \tag{2.6}$$

Equation 2.5 is the Orr-Sommerfeld equation for viscously strati ed ow, and equation 2.6 is the corresponding Squire equation. Notice that setting the viscosity to zero in the Orr-Sommerfeld equation reduces it to the Rayleigh equation. If this was done in cylindrical coordinates, we would follow a similar method, and would result in the additional possibility of helical modes.

Most often in stability analysis, the viscosity variation is neglected to simplify the system of equations. However, Govindarajan (2014) demonstrates how the stability characteristics of a ow can be highly dependent on viscosity and viscosity variation. First, viscous e ects can be large even for high-momentum ows due to the fact that they have a singular perturbation in the Orr-Sommerfeld equation (Drazin & Reid 1981, Lin 1946, Schmid & Henningson 2000). Viscous terms have an order one e ect

somewhere in the ow, regardless of the Reynolds number, and in these regions the viscous e ects cannot be accurately neglected. Intuitively, near a wall is of importance due to viscous wall e ects a ecting the ow pro le. However, the critical layer (which is the location where the phase speed of the disturbance is matched to the base ow velocity, i.e. $U \quad c$) can also be an important region, where viscosity variation can be a major factor, demonstrating that viscosity variation may be a factor even in open ows (Craik 1969). In fact, Govindarajan (2004) shows that critical layer e ects are order $Re^{-1/3}$, which is higher order than wall e ects which are order $Re^{-1/2}$.

Viscous variation e ects can also be seen through consideration of the disturbance kinetic energy. Disturbance kinetic energy, is here de ned for our three dimensional ow as:

$$\varepsilon \quad \frac{1}{2}(\hat{u}^2 + \hat{v}^2 + \hat{w}^2) \tag{2.7}$$

The rate of change of the disturbance kinetic energy is the di erence between the production and the dissipation, stress transport, and surface tension e ects:

$$\frac{\partial \varepsilon}{\partial t} = P \quad D + T + S \tag{2.8}$$

Here, $P = \langle \hat{u}\hat{v} \rangle U'$ is disturbance kinetic energy production by Reynolds stresses, and $D = 1/Re \langle r\, u \rangle^2$ is the viscous dissipation. The stress transport T and surface tension e ects S are:

$$T = r \quad [\quad \frac{\langle u\hat{p} \rangle}{\rho} + 2\frac{\mu}{Re} r\, \varepsilon] \tag{2.9}$$

$$S = \frac{1}{We} \langle [\hat{v}(\hat{h}_{xx} + \hat{(h)}_{zz}]_{y=\hat{h}} \rangle \tag{2.10}$$

The inverse of the Weber number is zero in the case of miscible uids where there is not surface tension, and therefore S is zero. The stress transport T is net zero across y for miscible ows, but is nonzero locally. As the dissipation is inversely related to the Reynolds number, viscosity does contribute to damping of the disturbance kinetic energy (Hu & Joseph 1989). Yet, viscosity can contribute to the disturbance kinetic energy production, sometimes to even a greater respect (Govindarajan 2014). The production is zero when $\hat{u}$ and $\hat{v}$ oscillate out of phase. The locally nonzero stress transport e ects T work to di use momentum across the ow, in uencing the phase relationship between $\hat{u}$ and $\hat{v}$, and impacting the disturbance kinetic energy production. Therefore, the disturbance kinetic energy production is another way that viscosity and viscosity variation can have an important role in uid stability.

Stability analyses most often show that viscosity strati cation leads to enhanced destabilization, as reviewed for bounded ows in Govindarajan (2014). Unidirectional immiscible two- uid wall-bounded ows of constant shear stress have neutral stability, but with the introduction of viscosity strati cation, they become unstable at any Reynolds number (Yih 1967). The predicted viscosity-dependent stability nature of such planar ows has been experimentally observed, rst in an oil-water experiment by Kao & Park (1972). The destabilizing e ect of viscosity strati cation has also been documented for immiscible core-annular pipe ow using theory (Hu & Joseph 1989), experimentation (Aul & Olbricht 1990) and simulation (Kouris & Tsamopoulos (2002). Similar ows have have been studied with miscible uids as well. Ranganathan & Govindarajan (2001) studied miscible core-annular channel ows, and determined that viscosity strati cation within the critical layer has a large stability response. Core-annular miscible pipe ow has also received signi cant attention, with viscosity strati cation resulting in either stabilizing and destabilizing e ects depending on the precise viscosity eld (Selvam et al. 2007), which was further con rmed through visualization by Cao et al. (2003).

Yet, the vast majority of ow situations with viscosity variation have not yet been studied. In particular, the above experiments were all performed on wall-bounded ows, which form only a small subset of common laboratory and engineering ows. No study has so far systematically investigated the e ect of viscosity strati cation in open ows, a topic which is started by this work with the study of a variable viscosity jet ow.

2.2 Pertinent Experimental Work

As stated in Section 2.1.1, flows can transition from convective to absolute instability with changes in velocity profile or other fluid characteristics. For spatially developing flows, this can mean transition into a globally unstable system. A number of important experiments have demonstrated such transitions in open flows.

Experiments first clearly documented this transition in wake flows. Mathis et al. (1984) and Strykowski (1986) experimentally demonstrated that the von Karman vortex street results from a global instability. The transition was triggered by carefully raising the Reynolds number above a certain critical value, after which the flow dramatically transitions into the self-sustaining vortex shedding mode. This was documented by transiently observing the magnitude of the velocity fluctuations growing exponentially upon a step increase to the Reynolds number, corresponding to the previously stable flow transitioning into the cyclical von Karman street. This transition was shown to be controllable through additional parameters such as heating (Noto et al. 1985, Mori et al. 1986, Strykowski 1986, Strykowski & Sreenivasan 1990, Lecordier et al. 1988), the presence of a small cylinder located near the wake region (Strykowski 1986, Strykowski & Sreenivasan 1990), and through mechanical oscillations (Berger & Schumm 1967).

The presence of global modes in jets has also been well documented. Monkewitz & Sohn (1988) calculated that homogeneous incompressible axisymmetric jets are convectively unstable everywhere. However, they additionally showed that local regions of absolute instability exist for jets with low jet-to ambient density ratios (ρ_j/ρ_1). The breakdown of low density jets has since been studied in a number of separate ways. Kyle (1988) used helium-nitrogen mixtures to obtain variable-density jets, a method that was built upon by Sreenivasan et al. (1989) who observed an unstable global mode for sufficiently low-density round jets obtained by mixing helium and air to specific ratios. Monkewitz et al. (1990) used heated gas to create low-density jets, and found the same global mode as Sreenivasan et al., and furthermore discovered another unstable mode at a higher critical density ratio. Other than the density ratio, additional parameters have been shown to influence the stability of jets. Kyle and Sreenivasan (1993) also included jet shear layer momentum thickness as a contributing factor for unstable modes. Additionally, they observed an apparent shutoff of the unstable mode at high Reynolds

numbers that was not explained with inviscid linear stability theory. This shuto may stem from a number of reasons, including misalignment of density and velocity shear layers at high Reynolds number, but a possible reason is that viscosity plays a role in jet stability. In a study of low-density nitrogen-helium jets, Hallberg & Strykowski (2006) used variable-length extension pieces on the end of a nozzle to allow manipulation of the jet boundary layer thickness independent of the Reynolds number. They concluded that the density ratio, Reynolds number, and jet diameter to momentum boundary layer thickness ratio are all independent variables for the onset of unstable global modes. In their investigation, they included a viscous timescale, yet did not consider di usion and viscosity variation within the jet (Sc = 1).

The onset of global modes in variable density round jets were found through the experiments of Sreenivasan (1989) and Hallberg & Strykowski (2006) to match with linear stability theory. Yet, the observation of global mode shut-o at high Reynolds number cannot be explained by inviscid stability theory. Calculations by Srinivasan et al. (2010) include a constant viscosity, and do perform better, yet they still do not fully explain the observed shut-o . Therefore, it is conjectured that e ects such as transverse di usion alter the viscosity pro les in the jet. The viscosity gradients may then stabilize or destabilize the jet as described in the previous section. No study has yet systematically studied the e ect of viscosity ratio on jet stability in an e ort to investigate this.

As far as the experimental technique is concerned, the above experiments demonstrated that having an initially laminar jet shear layer and a very low-noise facility are important. The experimental signposts for global instabilities include amplitude changes in velocity uctuation, highly peaked velocity uctuation spectral plots, and changes in behavior observed by jet visualization. Therefore, this study focuses on these three areas for the investigation of the in uence of viscosity ratio on round jets.

In this background, it was rst shown that viscosity strati cation has an important role in linear stability theory, even at high Reynolds number ows. Then, studies from wall-bounded ows demonstrated how these viscous terms have been documented to have major stability-altering e ects in laboratory ows. Finally, experimental work with spatially developing ows has given an idea on how global modes are seen in open ows and upon which parameters they are expected to depend. This background

information is leveraged in the following Motivation and Goals section, where the scope of the present work is given.

Chapter 3

Motivation and Goals

The present study seeks to add viscosity effects to the understanding of axisymmetric jet breakup. To do this, the variables of interest are defined, a measurement plan is developed, and a new experimental facility is created. The overall objectives of the study are then given.

The breakdown of an axisymmetric jet has been shown in the previous section to be dependent on density ratio, Reynolds number, and momentum thickness. This study adds the additional independent variable of viscosity ratio. In order to keep the study within control, several simplifications are made. The density ratio is eliminated through use of density-matched jet and ambient fluids. Only a single nozzle is used, so that the momentum thickness simply becomes a function of the Reynolds number. Miscible fluids are chosen so that no surface tension effects are present. Therefore, the only controllable variables are the jet Reynolds number and the jet-to-ambient viscosity ratio. The jet Reynolds number is defined on a flowrate basis of the fluid exiting the nozzle, and the viscosity ratio - denoted by M - is defined as the ratio between the viscosity of the far-field ambient fluid to the viscosity of the jet centerline.

A measurement plan is chosen to enable acquisition of measurements that can be compared with stability calculations, while also allowing independent observation of jet breakdown. To fulfill these requirements, the two techniques of hot film anemometry and flow visualization are selected. Anemometry is capable of measuring velocities over very small time intervals, allowing accurate acquisition of velocity fluctuations. These fluctuations allow direct comparison with unstable modes predicted through linear

stability theory. No predictions presently exist, but they are currently being worked out in the same lab as this work under the direction of Dr. Srinivasan. As such, the goal of the anemometry measurements is to accurately document the velocity uctuations for later comparison with theory. Secondarily, ow visualization is applied for the qualitative evaluation of the jet. As mentioned in the background, jets have exhibited dramatic changes in form due to unstable modes created by density di erences. The visualization here attempts to capture the form of the jet in order to discern if a viscosity ratio can impact jet breakdown in a similar fashion.

The creation of a facility capable of producing such a jet ow and taking such measurements is of paramount importance to this study. The requirements of the facility are that it must introduce a laminar jet into a quiescent ambient region, this jet must be initially free of environmental disturbances, and that it must allow visualization and hot lm anemometry measurements to be taken in a precise and repeatable manner.

In order to cover a suitable parameter space in this study, the jet is operated over a sizable Reynolds number and viscosity ratio range. The Reynolds number is de ned for the jet as:

$$Re \quad \frac{U_{\text{ave}} D \rho}{\mu_{\text{c}}} \tag{3.1}$$

where U_{ave} is the average jet velocity at the jet exit plane, D is the diameter of the nozzle tip, ρ is the density of the jet uid, and μ_{c} is the centerline jet viscosity. In this work, the Reynolds number is varied from 500 to 2000. This range was limited on the low end due to anemometry measurement di culty at lower jet velocities and at the high end by the requirement that the jet is initially laminar. The jet-to-ambient viscosity ratio M:

$$M = \frac{\mu_{\text{ambient}}}{\mu_{\text{jet}}} \tag{3.2}$$

is varied between 1 and 50, and is limited on the high side by the base viscosities of suitable density-matched experimental uids, and is limited to be above unity by practical

experimental concerns of keeping the uid passages separate to avoid contamination, as well as the di culty in generating higher Reynolds number jets with a highly viscous uid. Full information on the reasoning behind these both of these parameter decisions is given in the following sections.

In short, the objectives of the present study are to:

Design and characterize an experimental apparatus capable of generating a viscosity strati ed circular free jet

Measure velocity in both spatial and spectral dimensions for Reynolds numbers of 500 to 2000, for viscosity ratios M = 1 to 50

Visualize the jet to observe breakup modes for Reynolds numbers of 500 to 2000 and viscosity ratios M = 1 to 50

Chapter 4

Apparatus

A custom experimental apparatus was fabricated for the purposes of the present study. The design creates a smooth laminar jet which flows into a quiescent ambient fluid, while allowing for anemometry measurements and visualization.

4.1 Fluid Selection

The isolation of viscosity effects relies on the ability to create a viscosity gradient while holding density uniform. This is because, as seen in the background, density ratios have strong influences on jet stability that would obscure the effect of viscosity. The majority of previous jet stability studies were performed using gaseous fluids. However, gasses do not typically show wide ranges in viscosity, and in order to set up a sizable viscosity difference between jet and surrounding, dramatic changes in temperature or obscure fluids would need to be used. The wide range in temperature would create large density differences, while the obscure fluids would be experimentally unrealistic. The author has not found any two gaseous fluids that have reasonable viscosity differences while being of the same density. Using liquids, however, readily allows for large viscosity ratios while opening up additional density matching techniques. Liquids can be doped with solutes that change their overall density, allowing for precise density control.

For this study, propylene glycol and water are used as the two fluids. Propylene glycol in its pure form has a viscosity of 0.042 Pa s, which is over 40 times that of water, and has a density of 1.036 g/cm^3, which is only a few percent above the density of water.

Industrial propylene glycol formulations, such as is used in this work, may have an even higher viscosity. Water is then doped with sodium chloride salt in order to match the density of propylene glycol to within a tenth of a percent. The two uids have additional qualities of experimental performance. Propylene glycol and water are readily miscible, which eliminates surface tension e ects. Furthermore, propylene glycol and water are both optically clear, which allows for straightforward ow visualization techniques. Finally, both uids are relatively inexpensive and available in large quantities. Liters of working uid are used for a single experiment, upon which the uids are irreversibly mixed. Therefore, economics becomes important in a general experimental feasibility sense. In summary, propylene glycol and water are chosen for their large viscosity ratio ($>$40), small initial density di erence (3%), ability to be density matched, miscibility, optical clarity, and low-cost availability.

The particular propylene glycol formulation used is Dowfrost^{TM} Propylene Glycol Heat Transfer Fluid purchased from Duragard Oil. This propylene glycol formulation is of industrial purity and contains additives for corrosion and rust inhibiting. As such, the density and viscosity varies from batch to batch. Therefore, the densities and viscosities are measured individually before each experiment, a technique that is elaborated on in chapter 5. Water is obtained form the lab tap supply. The uids are both used at room temperature.

4.2 Apparatus Design

The designed apparatus is shown in Figure 4.1. It consists of a nozzle to form a round jet, a clear ambient tank test section into which the jet exhausts, a uid reservoir for the purpose of supplying uid to the jet, and a set of ow lines and valves to direct the ow through the system. Surrounding the clear tank are the anemometry and imaging systems. A full description of each subsystem is given in the following subsections.

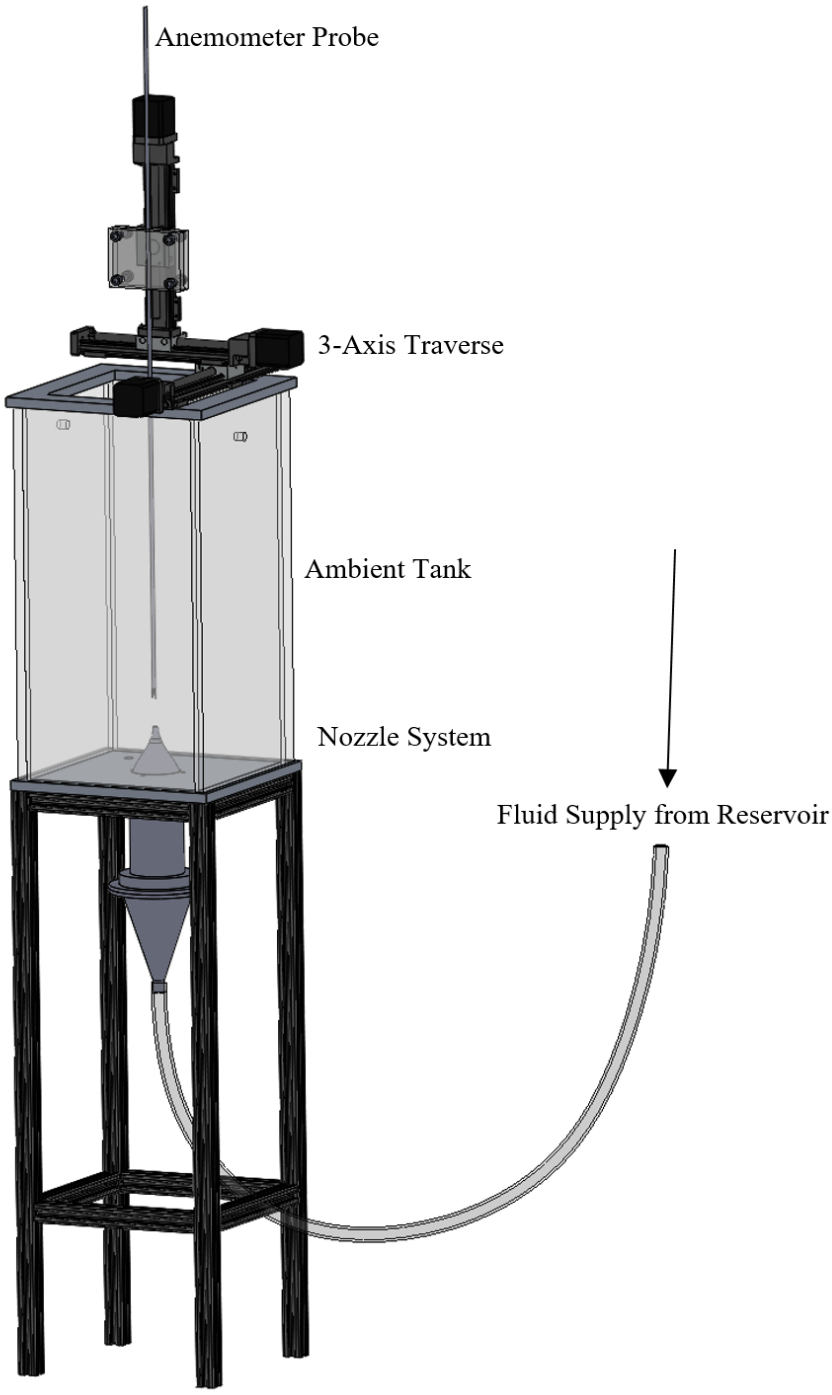

Figure 4.1: Experimental Apparatus.

4.2.1 Nozzle Assembly

The purpose of the nozzle assembly is to create a smooth laminar jet. Apart from the nozzle, the assembly also includes a di user and a ow straightener.

A drawing of the nozzle is shown in Figure 4.2. It is a fth-order polynomial nozzle with an area contraction of 87 to 1. The polynomial was chosen to have zero slope and curvature at both the entrance and exit. The entrance diameter is 5.6 cm and the exit diameter is 6 mm. The nozzle is 55 mm long, which was found through iteration to be the length resulting in the minimal boundary layer thickness and a uniform core velocity pro le. The nozzle was created using 3D printing. At the exit of the nozzle, the wall thickness is the smallest achievable by available 3D printers, which is 0.5mm. The actual nozzle diameter was veri ed by gauge pins, and was found to be 5.97 0.03 mm after fabrication. We de ne the coordinate z to begin at the nozzle exit plane and measure distance downstream, where the coordinate r measures the radial distance out from the jet centerline.

Located before the nozzle is a ow straightener. The purpose of the ow straightener is to break up any large scale structures in the ow. It is designed as a hollow cylinder measuring 12 cm long and 5.6 cm in diameter, with the inside volume lled with straws of diameter 0.6 cm. The straightener was machined from aluminum. It is attached to both the nozzle and the di user using ange connections sealed with gaskets.

A di user is located before the ow straightener and nozzle, and is used to expand the ow from the tube diameter to the ow straightener diameter. The di user is 25.2 cm long, diverging from a 1.9 cm inlet to a 5.6 cm outlet, so that the angle of divergence is 6 degrees. The di user was fabricated using 3D printing. At the entrance of the di user is a perforated plug, which serves to break up the developed tube velocity pro le of the incoming uid. The di user is shown in Figure 4.3.

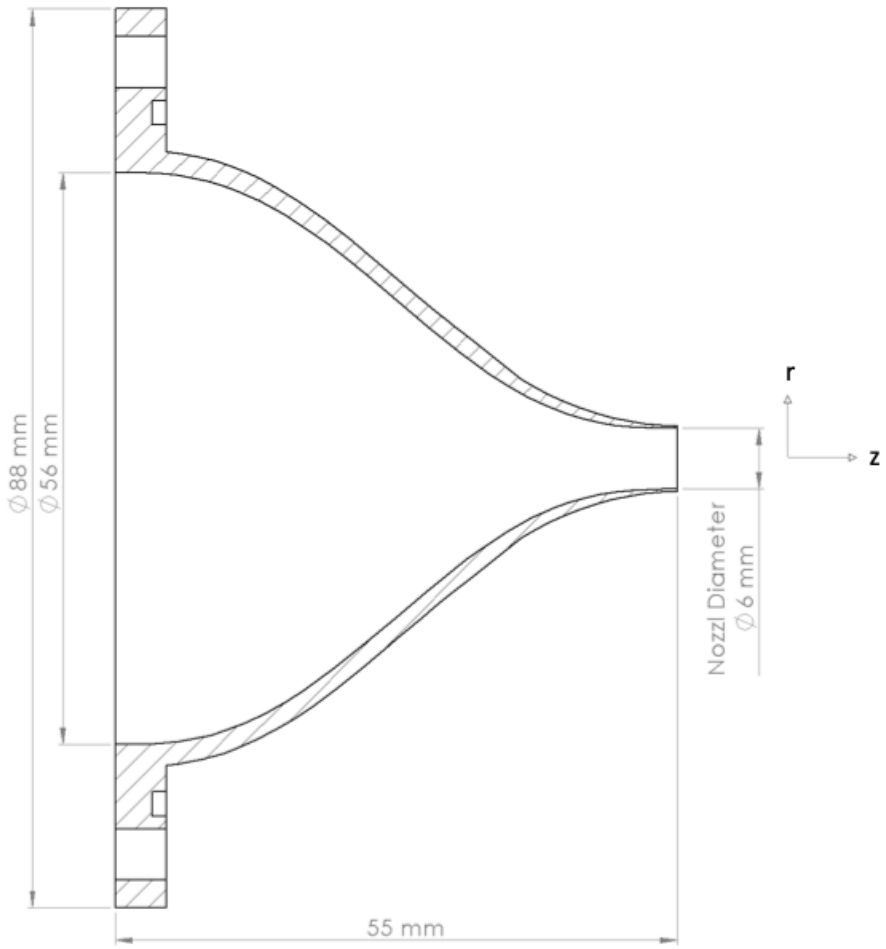

Figure 4.2: Section view of the nozzle used to generate the round jet. The z coordinate is measured downstream from the exit plane of the nozzle, and the r coordinate is measured radially outwards from the centerline of the nozzle.

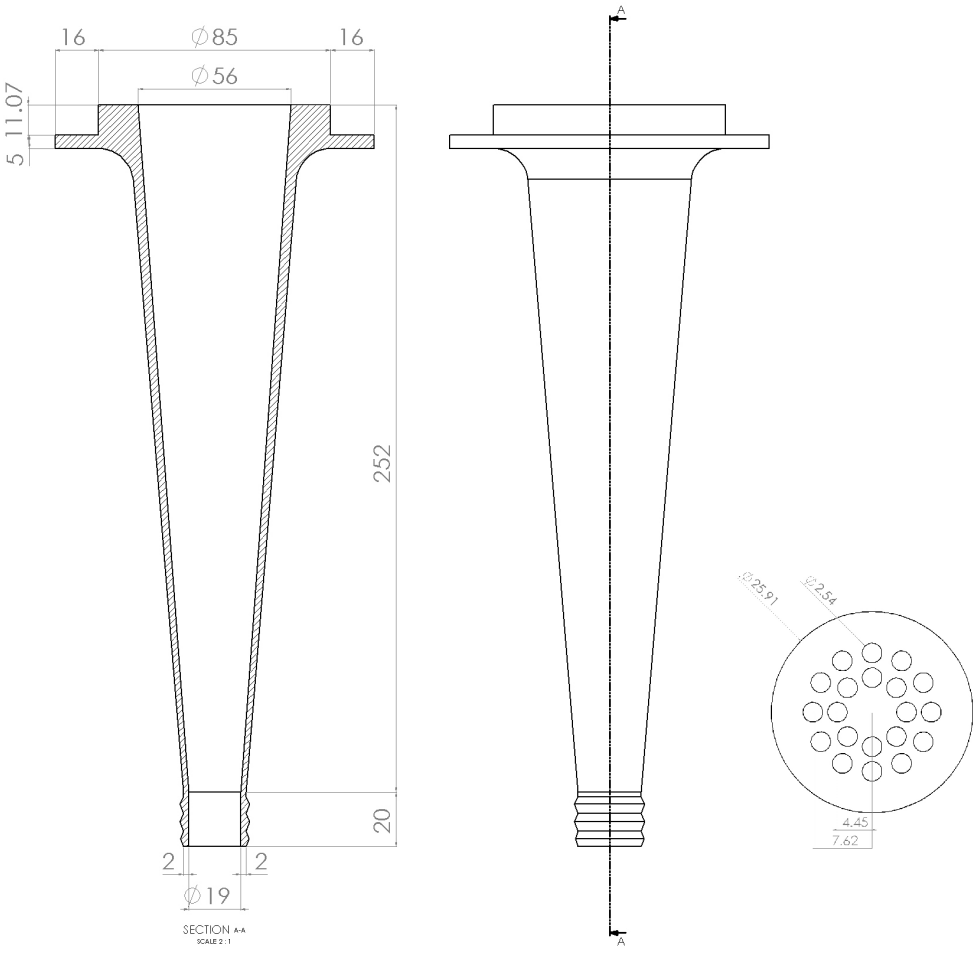

Figure 4.3: Drawing of the di user, showing a section view with dimensions (left), an outer view (center), and the perforated plug (right). All dimensions are in mm. Flow enters at the bottom and decelerates before owing up into the ow straightener.

4.2.2 Reservoir and Flow System

A large 20 liter reservoir contains the uid for the jet. It is located 1.5 meters above the top of the tank and thus provides the pressure required to force the ow. A pressure driven ow is desirable, in that it does not introduce vibrations into the ow as would a pump. The use of pressure does, however, introduce an additional experimental complication, in that changes in the height of the uid in the reservoir augment the available pressure, which in turn in uences the owrate of the jet. Therefore, the tank is chosen to have a much larger cross sectional area than the jet (D 1000) so that over the duration of each experimental run the change in pressure head is negligible.

The reservoir is connected to the nozzle assembly through 1/2" tygon tubing with an intermediary owmeter and cuto valve. From the bottom of the reservoir, the tubing rst runs down to a table-mounted variable-area ow meter. Use of a variable-area owmeter allows for control of the owrate using a knob. The ow meter measurement range is from 40 to 660 ccm with an accuracy of 3%. This ow range corresponds to saltwater jet Reynolds numbers of 130-2200. After the owmeter, a short run of tubing connects to a ball valve, which is used as the primary on/o control for the jet. Additional tubing then connects the the valve to the bottom of the di user.

4.2.3 Test Section

The test section is an ambient tank that holds quiescent uid into which the jet exhausts. The walls of the rectangular tank are 20 jet diameters radially from the jet, and the height of the uid in the tank reaches 65 jet diameters from the nozzle exit. The tank holds 25 liters of uid. The large size of the tank allows an in nite medium approximation to be applied to the ambient uid. The walls of the tank are made from clear acrylic to enable visualization. Furthermore, the top of the tank is open to allow direct mounting of an anemometry system. There are two exit ports near the top of the tank on opposing walls to allow symmetric over ow from the tank, so that a constant uid height is maintained in the tank even with uid input from the nozzle. The tank bottom is machined from aluminum, and includes a large central hole allowing the entrance of the nozzle, as well as a smaller side hole for an exit drain so that the tank can be emptied after the conclusion of each experiment. Four evenly spaced bolts

secure the nozzle to the tank bottom, with a gasket ring providing sealing. Additionally, sealing washers are used on the bolts to prevent the bolt-hole leak path.

The jet enters the tank vertically in order to limit the influence of possible density differences. If the jet were to enter the tank horizontally, small errors in density matching would result in the jet deflecting upwards or downwards. By orienting the jet vertically, the linearity of the jet centerline is ensured.

4.2.4 Anemometry System

A hot film anemometry system is used to take jet velocity measurements. The anemometry system is composed of a probe, a stem, a traverse assembly, the associated anemometer and multimeter electronics, and a computer program for control and data logging.

The probe used is a TSI hot film probe model 1260A-10W. A hot film probe is used instead of a hotwire probe due to the robustness needed for use in a liquid flow. Use of hot film probes in liquids can cause a voltage difference to build up between the probe and the liquid, due to electric charges in the flowing liquid. This voltage difference can break down the quartz coating of the probe and cause premature failure. As a preventative measure the aluminum bottom of the tank and the metal flow straightener are wired to building ground.

The probe attaches to a straight stem, which is held above the tank by a 3-axis traverse system. The probe stem is oriented parallel to the jet flow direction. Flow visualization confirmed that the probe oriented in such way provides minimal disturbance to the jet. A straight stem is chosen to allow the stem to exit at the open top of the tank, where it attaches via a custom clamp to the three axis traverse system (Velmex XSlide Linear Stages). Frequency analysis shows that the stem and clamping system eliminate vibrations in the stem that could introduce erroneous fluctuations in the velocity measurements. The traverse system is bolted to the top of the tank walls in order to keep it in a fixed location at all times. Each linear traverse has 76 μm straight line accuracy, which is 1% of the jet diameter. The traverse system is controlled by a motor control box (Velmex VMX Stepping Motor Controller) and responds to computer input.

A constant temperature anemometer (TSI IFA 100) is used to control the probe and to obtain the desired voltage data. The voltages are then passed to a digital multimeter

(Agilent 34411A). Voltage measurements are read from the digital multimeter into a computer.

A single custom Python script is used to simultaneously run both the traverse system and to record the output of the digital multimeter.

4.2.5 Visualization System

Fluorescent dye imaging is used for flow visualization. The fluorescent dye used is Rhodamine B. Through experimentation it is determined that 0.1 g of Rhodamine B is sufficient to dye the 20 liter reservoir. Insufficient dye concentration will not enable viewing of the jet, while too much dye will cause build up of residual dye in the ambient tank and obscure the jet in future trials. Rhodamine B dye absorbs light at wavelengths near 550 nm (green), and will fluoresce at 630 nm (orange). An LED (ILA Gmbh) is used to generate green light. The LED is used both openly and as directed into a light sheet. The camera used is a Canon EOS Revel T2i. The camera is typically placed at a right angle to the LED so that the full cross section of the jet is observed. The imaging is done under darkness in the room, so that the only light incident on the camera is the light emitted from the dye. Images are post-processed with the software ImageJ, in order to increase contrast between the jet and the dark background. Figure 4.4 shows the orientation of the LED and camera.

A hydrogen bubble imaging system was also created and used. However, an advantage of dye imaging is that the dye does not introduce any disturbance into the flow, so that the true nature of the flow is recorded. Furthermore, the hydrogen bubble method was difficult to use repeatably, as the extremely fine platinum wire ($25\mu m$) broke easily.

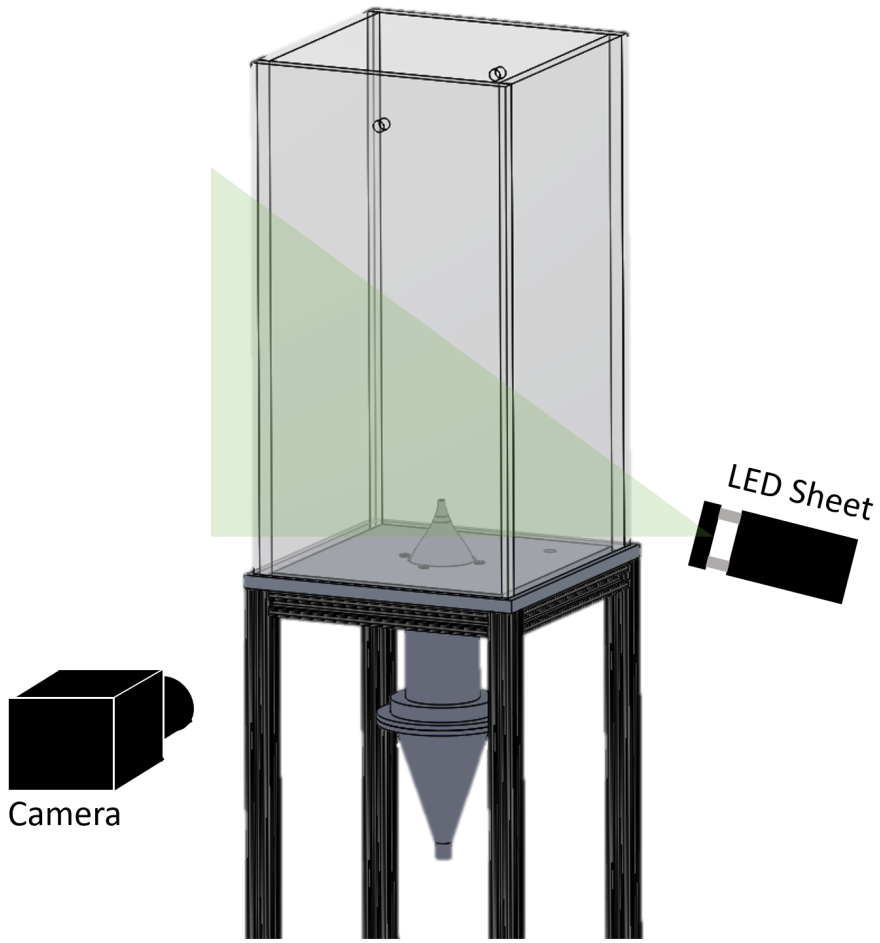

Figure 4.4: Flow visualization camera and LED position

Chapter 5

Experimental Technique

Each experiment requires the preparation of density matched uids, the apparatus setup and operation, acquisition of either hot lm anemometry data or visualization images, and testing of the uid properties. Each of these steps is expanded upon in the following sections.

5.1 Density Matching

In order to eliminate density ratio e ects, the density of water is matched to the density of propylene glycol by the addition of salt. First, the speci c gravity of propylene glycol is measured using a hydrometer (accuracy 0.0005). The density of propylene glycol is near 1.043 g/cm^3 but can vary slightly depending on the batch. The reservoir is then lled with water, and salt added. A paint mixer (HDX 5 gallon Helix Paint Mixer) connected to a hand drill is used to rapidly mix the salt into the water. Su cient time must be given for the air bubbles to escape and the correct speci c gravity to be measured by the hydrometer. Density adjustment by adding salt or water continues until the saltwater matches the propylene glycol within 0.001 for speci c gravity.

5.2 Experimental Setup

Experimental setup includes connection of the ow lines, introduction of the uids, and initialization of the anemometry or visualization systems. First, the density-matched

saltwater reservoir is placed above the apparatus. The tubing is then connected between the reservoir and the owmeter, between the owmeter and the shuto valve, and from the shuto valve to the bottom of the di user. The shuto valve is then opened and the saltwater is run through the lines until it reaches the nozzle exit plane, at which point the shuto valve is closed. Propylene glycol is then added to the ambient tank. The tank lling is best performed with the aid of a siphon, so that bubbles are not created in the tank due to air entrapment during pouring. At this point, the jet is ready to operate, by opening the shuto valve and setting the owmeter to the required value. The anemometry or visualization systems are then setup and run in the methods described in the following sections.

5.3 Imaging Technique

The imaging experiments begin with density-matching the uids and preparing experimental setup. Additionally, 0.1g of Rhodamine B dye is added to the jet uid reservoir. The light source and camera are then positioned and turned on. Typically the camera is set at a 90 angle from the light source, so that a light sheet can be used to illuminate a cross section of the jet. The camera shutter speed is set to be su ciently fast so that it freezes the motion of the jet. The shutter speed is typically set to 1/250th of a second. The experimental trials are then performed by turning the shut-o valve to open to start the ow of the jet, waiting ve seconds for the starting vortex to convect away and for the jet to reach steady state, and then taking picture bursts for the desired amount of time. After each trial, the uid in the tank is mixed thoroughly before a density measurement is taken and a viscosity sample is obtained for later testing. An additional complexity in the visualization experiments is that dye builds up in the tank over time, reducing the relative visibility of the jet. Low viscosity ratios are therefore achieved by mixing additional un-dyed, density-matched saltwater directly into the tank in between trials.

5.4 Anemometry Technique

The overall purpose of the anemometry experiments are to document flow velocities and fluctuations as dependent on jet Reynolds number and the viscosity ratio. Hot film anemometry measurements are dependent upon orientation of the probe in the flow. As stated in Section 4.2.4, the probe stem is oriented parallel to the x-direction. This means that any flow in the radial direction is not measured, which is an allowable simplification due to the near-nozzle jet flow being essentially unidirectional. Anemometry technique involves both calibration, and the taking of velocity measurements in the jet at various jet Reynolds numbers and jet-to-ambient viscosity ratios.

In order to account for exact experimental conditions, the probe is calibrated immediately prior to every experiment. The calibration is performed using the generalized King's Law, which relates measured voltage to a known velocity.

$$E^2 = A + BU^{1/n} \tag{5.1}$$

In Equation 5.1, E is the voltage from the anemometer, U is the flow velocity, and A, B, and n are coefficients fit to best linearize the voltage data.

Hot film calibration is performed directly in the experimental apparatus using the flowmeter and nozzle. The known flowrate going through the flowmeter is equal to the flowrate through the nozzle exit. Therefore, the average velocity through the nozzle exit can be calculated from the flowrate, and used as the velocity reference for the calibration. However, the jet velocity profile is not uniform, as there exists a sizable boundary layer. This boundary layer would cause underestimation of the true centerline velocity if a uniform velocity approximation was used. As a way to decrease error, the calibration is augmented using a volume-matching technique, where coefficient B in Equation 5.1 is tweaked until the volumetric flowrate calculated from measurements of the jet profile matches the flowrate determined from the flowmeter. The full details of the calibration technique is given in Appendix A.

All parameters involved in running the anemometry system are controlled in a Python program. Important parameters include measurement frequency, duration of

measurement at each location, and the probe measurement locations as determined by the traverse system. The measurement frequency is typically set to 1000 Hz, which is more than an order of magnitude higher than the velocity uctuation frequencies of interest. The duration of measurement time at each location is at least one second, so that low frequencies are adequately captured. The probe locations are set using commands to the traverse system. In trials where the probe travels to a number of positions in succession, at least two seconds of delay are added between the probe reaching a new location and the measurements beginning, so that disturbances in the ow created by the movement of the probe have time to convect away.

Each experimental trial is begun by turning on the jet using the ball valve and immediately starting the computer program. The program has an initial ve second delay to allow the jet to reach steady state and to allow the starting vortex to convect away. During this delay, the anemometer is switched from standby mode to on. The computer program will then automatically control the movements of the probe and perform data collection. At the conclusion of the trial, the ball valve is closed and the anemometer is turned to standby mode, to prevent probe overheat in the still uid. The tank now contains the propylene glycol viscous uid and the saltwater that was just exhausted into the tank. These uids are mixed together using the drill-operated paint mixer for one minute. A measurement of the tank uid density is then taken using a hydrometer. Also, a 15 mL sample of the tank uid is collected for later viscosity testing. The tank is given su cient time to come to rest before the start of the next trial. In this way, experiments progress from high viscosity ratios to low viscosity ratios, due to the tank viscosity lowering through the growing ratio of saltwater to propylene glycol. The particular viscosity ratios tested are a result of the volume of jet ow exhausted into the tank during each trial. Target viscosity ratios are achieved by allowing the jet to run at a particular owrate for a speci ed amount of time in order to hit a particular desired saltwater concentration.

After each experiment, the tank uid samples and a jet saltwater sample are tested in a TA Instruments AR-G2 rheometer for determination of viscosities. Additionally, after each experiment the hot lm probe is cleaned. This is necessary as the quartz coating of the probe accumulates calcium carbonate and other mineral deposits over time which can change the sensitivity and accuracy of the probe. Therefore a camel

hair brush dipped in DI water is used to carefully brush away deposits.

5.5 Error Analysis

The primary measurements taken are the jet owrate, the hot lm voltage and frequency, and the speci c gravity of both the jet and the ambient uid. These base measurements are then used to calculate jet velocities, and the frequency of the most unstable mode. The owrate was measured using a Brooks 40 to 660 ccm variable area mechanical owmeter (Model 2520A4L52SVVT), which has an error of 3% full scale. The Agilent 34411A multimeter used to measure the hot lm voltage has an uncertainty of 0.003% of reading and 0.0005% of range. As a minimum of 1024 voltage values are taken at a single measurement point, this corresponds to an overall voltage uncertainty of 6.32E-4 V. The speci c gravities are measured using a hydrometer with a resolution of 0.001, and the saltwater solution was prepared so that its speci c gravity matched the propylene glycol within 0.001. From these measurements, the corresponding error in the jet velocity is 7%, and the frequency of the most ampli ed instability has a resolution of 0.5 Hz. The derivation of these quantities, as well as a discussion of other possible sources of uncertainty, is given in Appendix B. By far the largest source of error is the uncertainty in the owmeter, and as such the use of a higher resolution owmeter is recommended for subsequent experiments.

Chapter 6

Results and Discussion

6.1 Characterization of Jet

The experimental apparatus is designed to produce a circular axisymmetric free laminar jet. Here we investigate the properties of the jet to confirm these attributes and determine the base flow characteristics for use in subsequent stability analysis.

A typical mean velocity profile is shown in Figure 6.1, as measured through hot-film anemometry. This profile is shown starting from the jet centerline outwards, at a downstream location immediately after the exit of the nozzle (z = 0.01D).

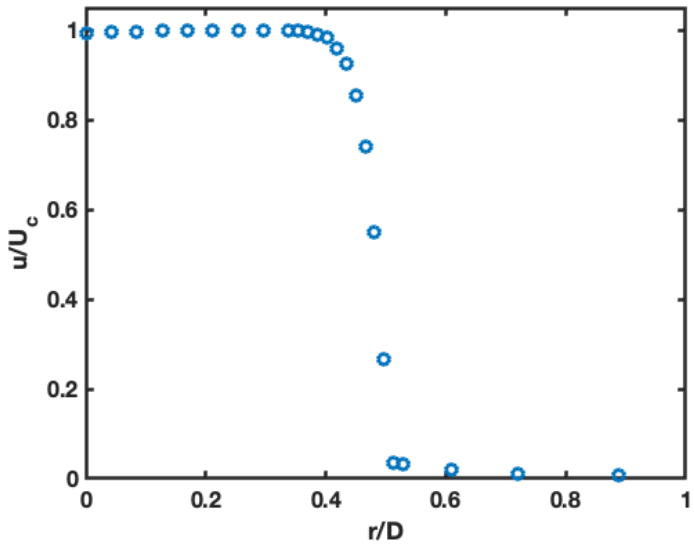

Figure 6.1: Typical velocity pro le of the base (M=1) jet, obtained at z/D = 0.04 and Re = 2000.

A typical turbulence intensity plot is shown next in Figure 6.2, over the same pro le as the previously shown velocity pro le. The core of the jet has an extremely low turbulence intensity of 0.1%, while a spike in turbulence intensity exists at the shear layer equal to 5% of the jet centerline velocity. The turbulence pro le spike in the shear layer is as expected for jets. The non-zero turbulence intensity outside of the jet indicates that the some turbulence generated in the shear layer extends out into the ambient uid.

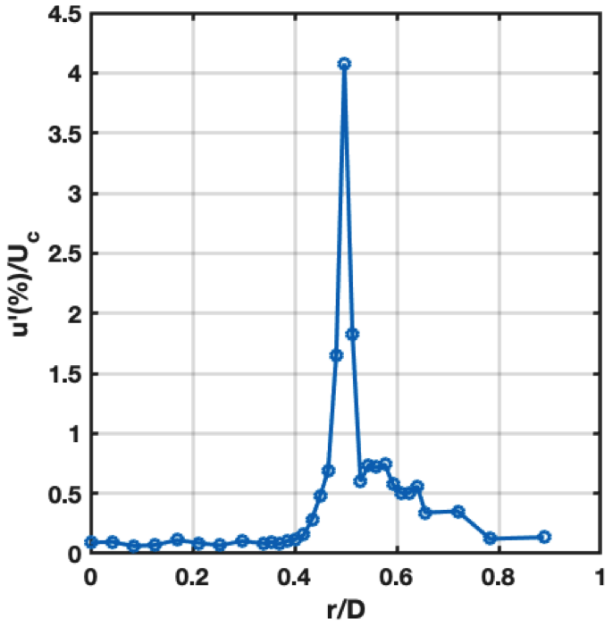

Figure 6.2: Turbulence intensity of the base jet (M=1) pro le over the radial extent, obtained at z/D = 0.04 and Re = 2000

The trends shown in these pro les are consistent with those presented in similar work with fth order polynomial nozzles, such as Drubka and Nagib (1981) and Niccum (1990). The pro les are shown in Figure 6.3 alongside pro les measured by Todde et al. (2009) in their work on low Reynolds number free jets (Re = 2700). It can be seen that the velocity pro le closely matches, and the turbulence intensity pro le has a comparable trend, although the current work has much lower centerline turbulence intensity. This speaks to the bene t of having a gravity-fed jet, free from any disturbances downstream from pumps or fans.

Figure 6.4 further investigates the initial disturbance level in the jet, by showing the spectral characteristics of the voltage signal as taken at the at the center point of the exit point of the nozzle (z=0,r=0). It is seen that no discrete peaks are present, which is an important attribute to avoid unwanted forcing inputs that could in uence the ow stability.

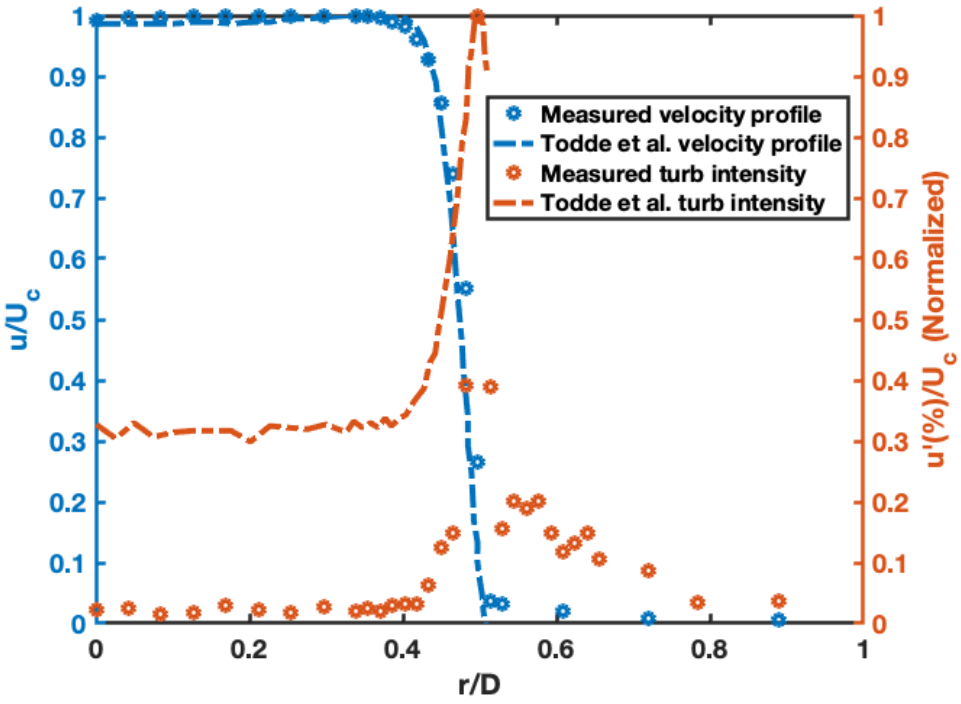

Figure 6.3: Velocity pro le and normalized turbulence intensity of the base jet (M=1) pro le over the radial extent, obtained at z/D = 0.04 and Re = 2000, compared to the values presented in Todde et al. (2009) for a similar M=1, Re = 2700 free jet ow.

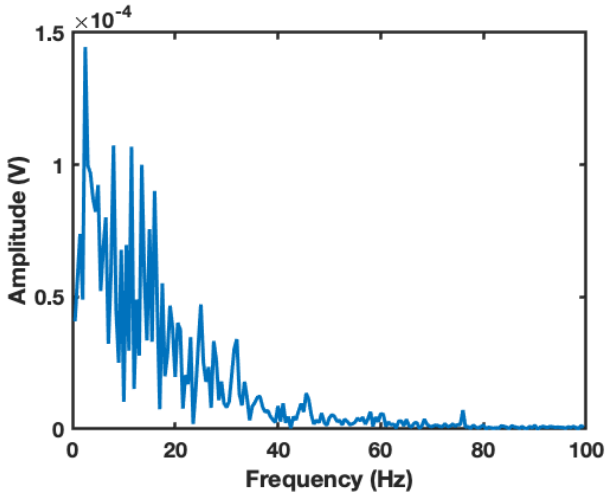

Figure 6.4: Spectral characteristics at the base jet (M=1) exit plane, obtained at z = 0, r = 0, and Re = 2000

Next, the boundary layer of the jet is investigated to characterize the particular nozzle and to determine whether the boundary layer exhibits behavior typical of a laminar jet. The boundary layer thickness is characterized using the momentum thickness, θ, which is de ned for a standard jet mixing layer as:

$$\theta = \int_{Y_1}^{1} (\frac{u}{U})(1 \quad \frac{u}{U})dy \tag{6.1}$$

Because hot lm anemometry cannot accurately measure ow at low speeds, Y_1 is used as the lower limit of the momentum thickness integral. Y_1 is de ned as the location where u/U_1 = 0.1.

For laminar boundary layers, we expect the momentum thickness to grow with the square root of the jet velocity. Figure 6.5 shows the relationship between the nondimensionalized boundary layer thickness with the square root of the Reynolds number.

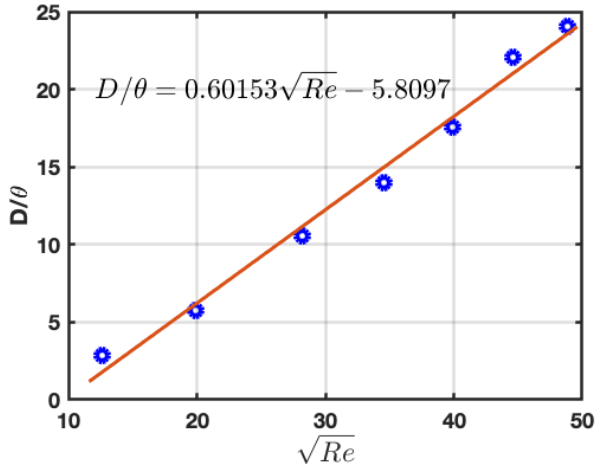

Figure 6.5: Momentum thicknesses nondimensionalized by the jet diameter over Re = 40-2400 at axial location z = 0.1D, with best fit line shown.

When normalized by the momentum thickness, the jet exhibits self-similar behavior as shown in Figure 6.6.

$$u = \frac{1 + tanh\left(\frac{D}{4\theta}\left(\frac{1}{r} \quad r\right)\right)}{2} \tag{6.2}$$

It can be seen in Figure 6.6, that at downstream locations very close to the nozzle tip, the profile is distorted due to tip wake effects. It is at the position of z/D = 0.208 where the jet has first become self-similar. This position is taken to be the origin of our mixing layer.

6.2 Characterization of Test Facility

The previous section pertained to the characterization of the base jet, as defined by a water jet entering a water-filled tank. In order to generate a viscosity gradient, propylene glycol is instead used in the tank. The characterization of the facility related to the water jet issuing into the propylene glycol environment is discussed in this section.

First, density effects are investigated. At the beginning of each experiment, the saltwater is density matched to the propylene glycol, as discussed in the technique section. However, propylene glycol-water mixtures do not maintain the same density

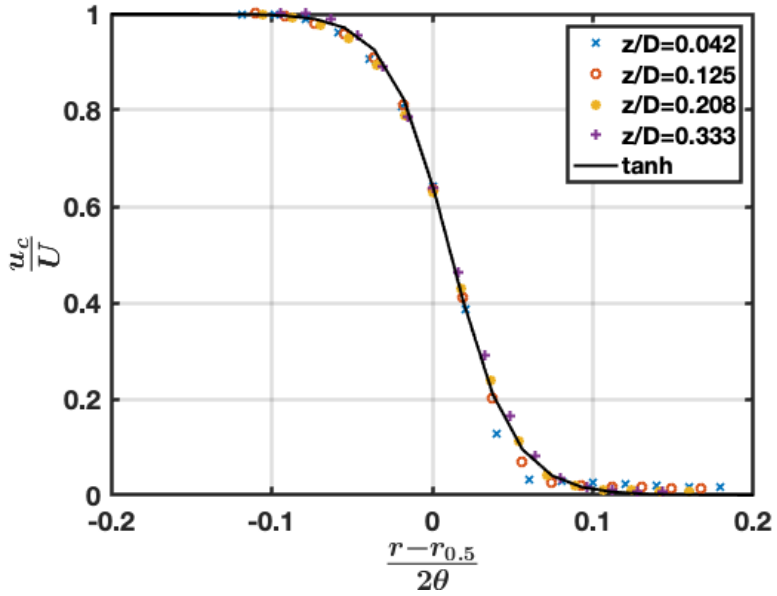

Figure 6.6: Normalized mean velocity pro les for the base jet (M=1) mixing layer at positions downstream. Obtained at Re = 2000.

as the base uids due to molecular e ects. These density changes are measured in order to quantify their e ect on the present study. The density-matched saltwater jet is exhausted into a pure propylene glycol environment in one minute increments. After each minute, the jet is stopped, and the tank is mixed thoroughly before the speci c gravity is measured and a sample is taken for later viscosity analysis. Figure 6.7 shows the results for this test.

As gure 6.7 displays, the density of the bulk PG water mixture in the tank is dependent on the water concentration. The speci c gravity varies between the 1.036 of pure propylene glycol to a maximum of 1.051. One way to quantify the e ect of this density di erence is through the Richardson number, a dimensionless number corresponding to the ratio of buoyancy to shear:

$$Ri = \frac{g \quad \rho D}{\rho V^2} \tag{6.3}$$

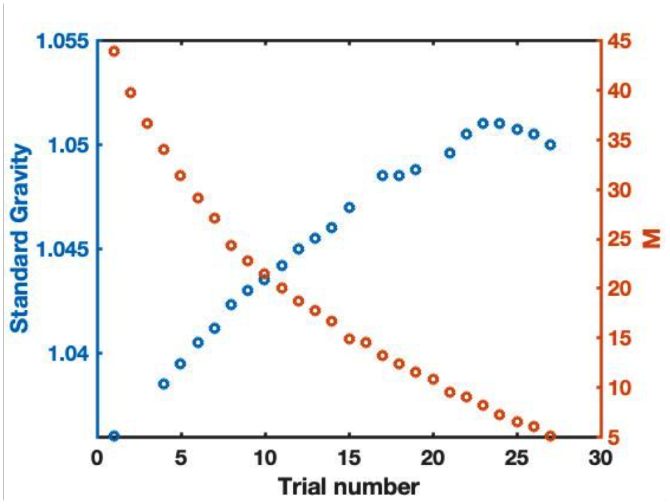

Figure 6.7: Speci c gravity and viscosity ratio (M) measured in the well-mixed tank after a series of jet ow trials, each lasting about a minute.

In Equation 6.2, g is acceleration due to gravity, ρ is the density di erence between the tank uid and the incoming jet uid, D is a characteristic length, for which we use the jet diameter, and V is the velocity of the jet. For the worst case condition, the lowest Reynolds number (670) is used for the largest density di erence:

$$Ri = \frac{9.81 m/s^2 \quad (1.051 \quad 1.036) \quad 0.006m}{1.036 \quad (0.12 m/s^2)^2} = 0.06 \tag{6.4}$$

The Richardson number of 0.06 means that the buoyancy e ects are 6% as important as shear e ects for this worst case condition. For the higher, Re = 1700 case the Richardson number is 0.03 at the worst case density di erence. Therefore, we conclude that - although the density di erence will have an e ect - it is small enough to exclude from the analysis.

Figure 6.7 also shows the ambient-to-jet viscosity ratio out the outset of each trial. Although it is measured in discrete points between trials, the viscosity condition apparent at the jet boundary is also continuously changing with time as the jet issues into the tank during each trial. A way to quantify the level of this change is to calculate the di usion length over the length of the trial. The di usion length is calculated by:

$$\text{Diffusion length} = \sqrt{Dt}$$

where D is the mass diffusivity of propylene glycol into water ($0.001123 mm^2/s$), and t is the time of the trial. For a one minute trial, the diffusion length is:

$$\text{Diffusion length} = \sqrt{Dt} = \sqrt{0.001123 mm^2/s \quad 60s} = 0.01 \text{ jet diameters}$$

Because this length is only 1% a jet diameter, it is seen that changes to the viscosity condition due to diffusion effects over a trial are small compared to the jet size.

Another way of looking at the viscosity condition change is through the Schmidt number, which is a ratio between the momentum diffusivity and mass diffusivity:

$$\text{Schmidt number} = \frac{\nu}{\mathscr{D}} = \frac{1.05e \quad 6 m^2/s}{1.23e \quad 9 m^2/s} = 853$$

The high Schmidt number of 853 shows that the mass diffusion is effectively minimized when compared to the momentum effects.

6.3 Flow Visualization

Visualization of the jet across Reynolds numbers and viscosity ratios is presented in this section for qualitative insight into the breakdown behavior of the jet.

Images of the jet breakdown for M = 1 are presented in Figure 6.8. These images show classic jet breakdown, with the axisymmetric Kelvin-Helmholtz cells forming in the shear layer, which grow and eventually break up the jet core. The jet breaks up more rapidly at higher Reynolds number, as expected.

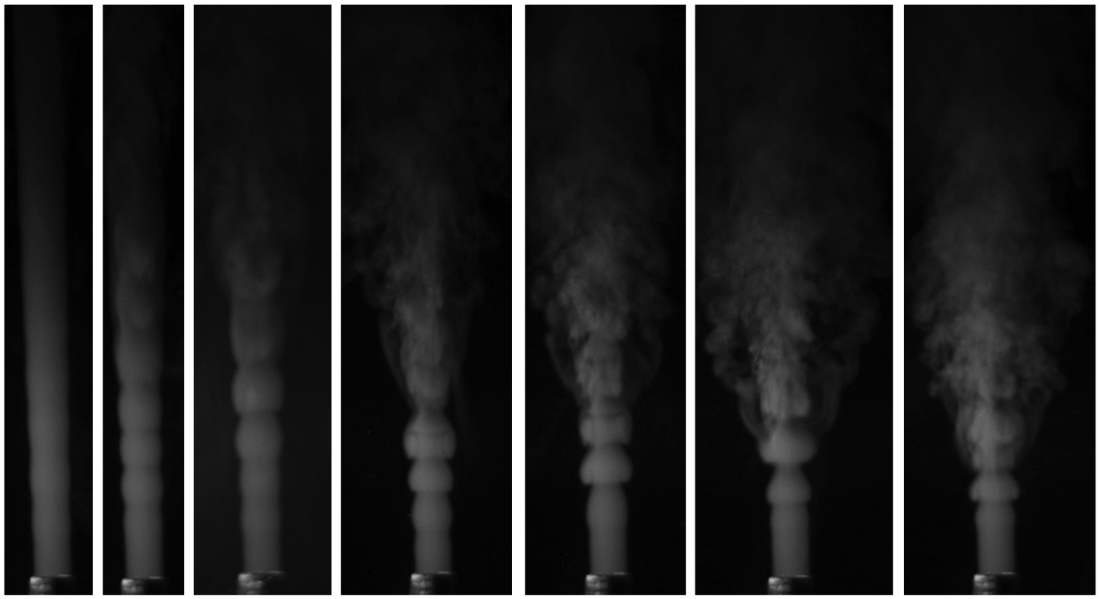

Figure 6.8: Images of jet breakdown for a range of Reynolds number. M=1.

In Figure 6.9, the breakdown of the jet is presented for a high viscosity ratio of M = 47. Note how an entirely new breakdown mode is observed. The breakdown displays a helical mode at high Reynolds numbers.

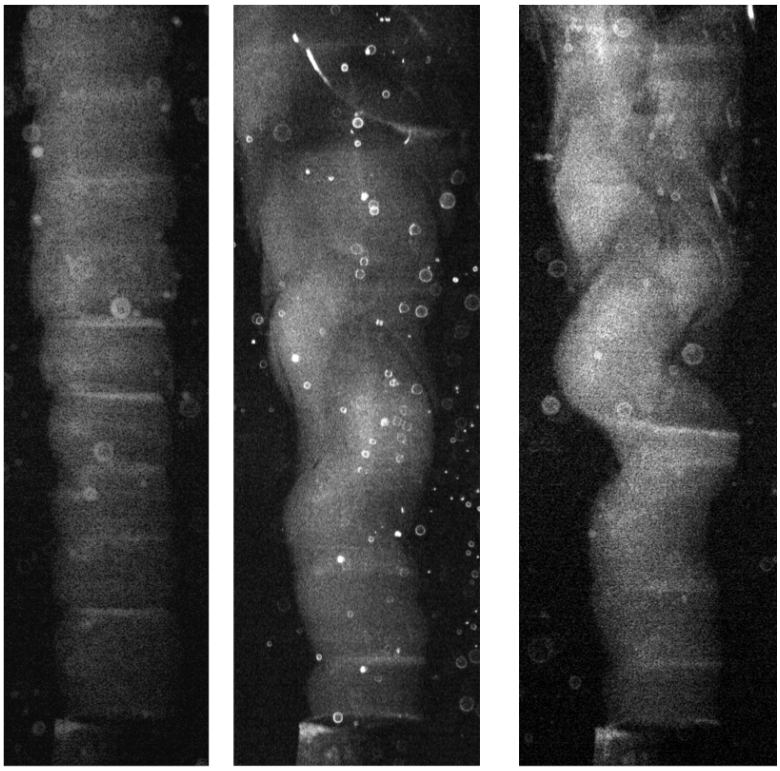

Figure 6.9: Images of jet breakdown for a range of Reynolds number. M=47.

Next, the jet images are shown in 6.10 for a range of viscosity variations for a single Reynolds number of 1077. The transition to a helical mode is again observed, this time for high viscosity ratios.

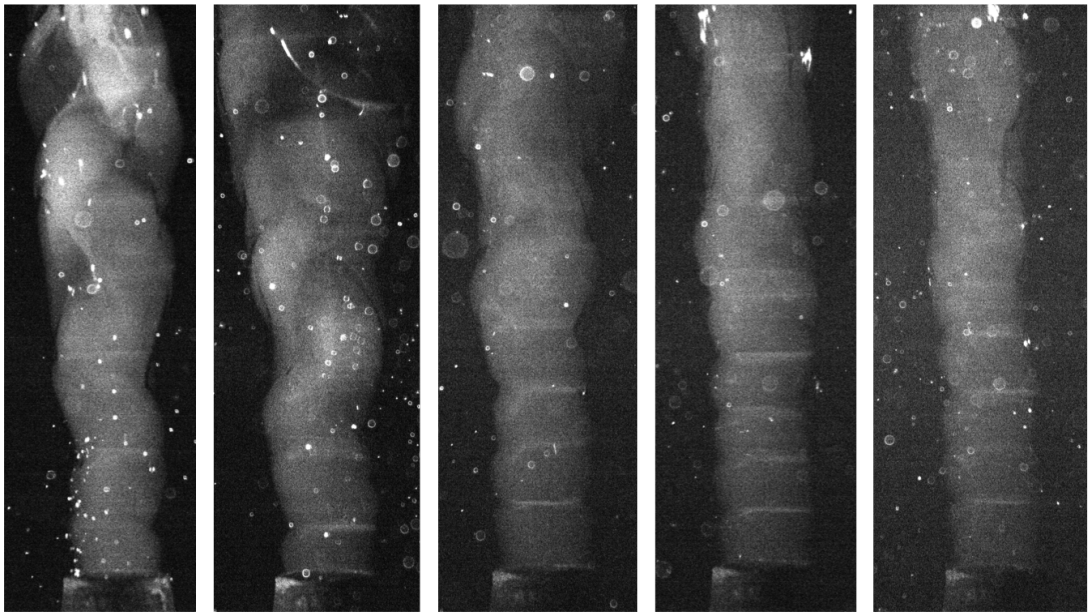

Figure 6.10: Images of jet breakdown for a range of viscosity ratios. Re=1077.

6.4 Jet Instability

In this section, the overall instability trends are first explored, before the spectral data are presented and discussed.

The development of the most unstable mode is first investigated. The hot film probe is placed at the jet centerline, and moved in increments of z/D = 1/6 from the jet exit plane until z = D. The results are displayed in Figure 6.11. Note how in the locations nearest to the jet exit, no unstable mode is clearly observable. At z=1/2D, a peak at a frequency of about 30 Hz is observed. This peak grows in amplitude in the further downstream locations. A digital high-pass filter is used on the spectral data, so that apparent long-wavelength disturbances do not obscure the trends.

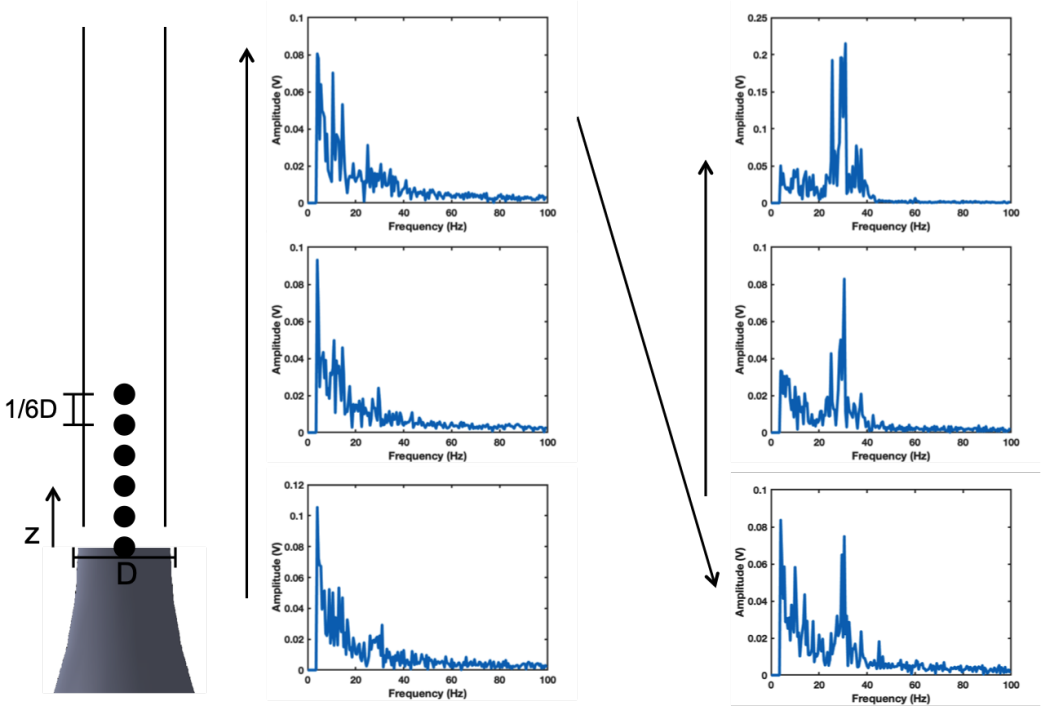

Figure 6.11: The spectral data from the early jet development. M=11, Re = 1682.

Next, the far downstream locations of jet are investigated to observe the decay of the unstable mode. The probe is positioned again on the centerline of the jet, but now at further downstream locations. The locations and spectral results are shown in Figure 6.12. Note how the spectral data clearly displays a peak at the rst location, before gradually becoming more broadband further downstream. The decay of the single oscillatory mode and the rise of broadband turbulence is as expected for a jet descending into turbulence.

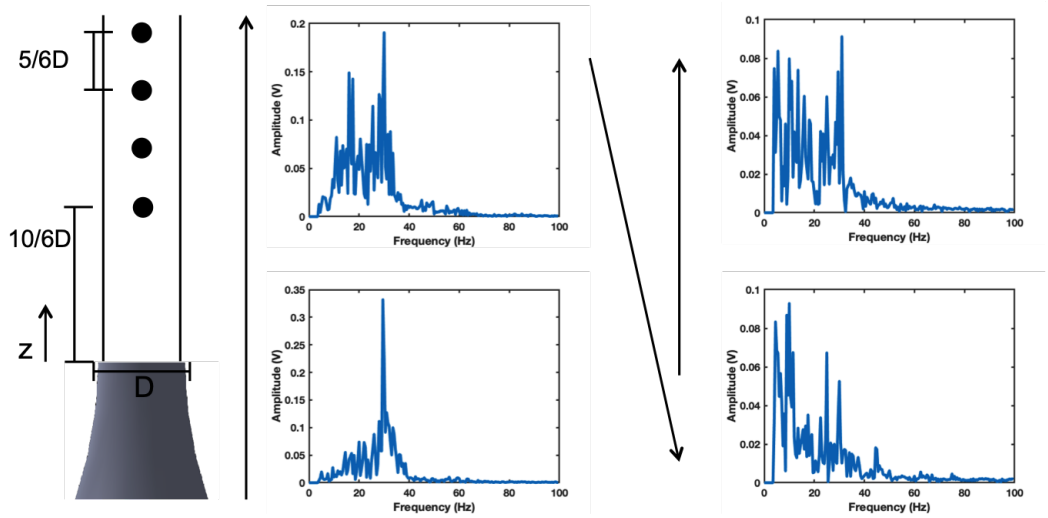

Figure 6.12: The spectral data from the later jet development. M=15, Re = 1682.

In order to further investigate the nature of the observed instability, the relative amplitude of the disturbance is next determined as related to jet location. Figure 6.13 shows the amplitude of the disturbance in the jet centerline and shear layer, at locations downstream of the jet exit plane. Note the rapid increase in the disturbance amplitude in the shear layer at the location z/D = 1.5. In Figure 6.13, the measurement resolution is one measurement every 1/6D. This measurement density results in an unacceptably long trial time of three minutes total, due to the two seconds measuring period at each location and two seconds of traverse time between locations. In order to cut the trial times to under a minute - as desired based on the viscosity di usion arguments made in the previous section - it was decided that a total of ten measurements (ve downstream locations, measuring in both the centerline and shear layers) were the optimal number of locations in a single test. These axial positions of these ve measurements were chosen carefully in order to still capture the full physics of the instability development. One point is tested before the observed development of the unstable mode (z = 1/6D), another location directly before the observed increase (z = 1D), one point in the middle of the increase (z = 8/6D), one point downstream of the increase (z = 2-1/2D), and one point far downstream (z = 4-1/6D). Black bars denoting these locations are shown in Figure 6.13, with the exception of the furthest downstream location which exceeds the bounds of the plot.

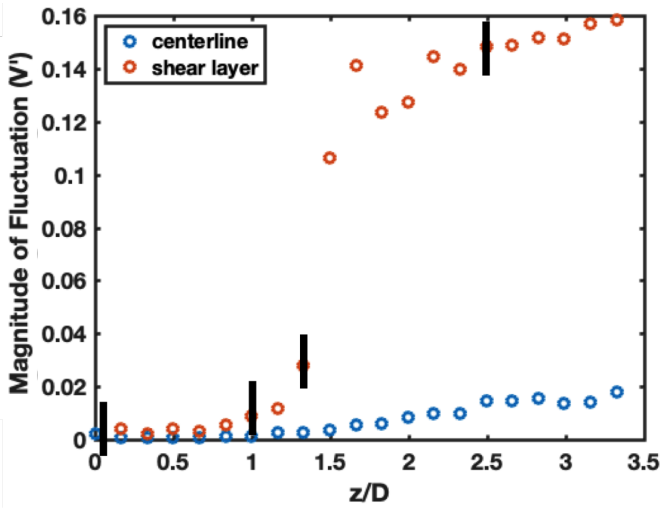

Figure 6.13: The amplitude of the disturbance is presented against the testing location downstream of the jet exit plane. M=11. The locations picked for additional frequency testing are marked with a black line. One additional location, at z/D = 4-1/6D, is not shown in this gure.

These ve locations are next investigated to demonstrated that they capture the instability pre-development region, the rise of the disturbance, and the saturation of the observed disturbance. Such a plot is shown for a high viscosity ratio case, M=27, in Figure 6.14. The rapid rise in disturbance amplitude is once again observed in the shear layer. The trend exhibited in Figure 6.14 is consistent in overall behaviour with observations for all high viscosity ratio cases.

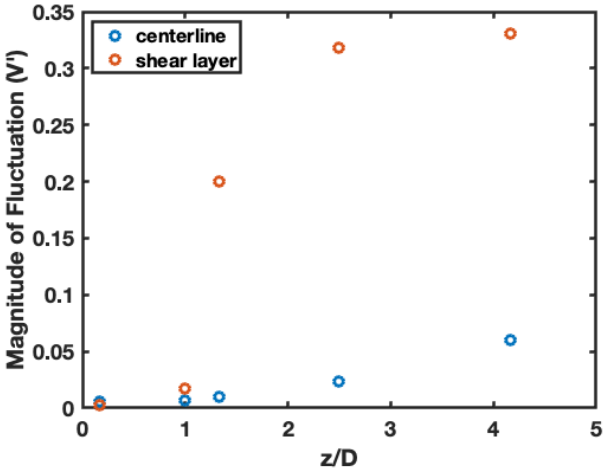

Figure 6.14: The magnitude of the measured hot lm voltage disturbance is presented against the ve chosen axial locations. M=26, Re = 1682.

The rapid rise in the shear layer disturbance amplitude observed in such high-viscosity ratio cases is contrasted with the disturbance amplitudes of a trial without a viscosity ratio (M=1) in Figure 6.15. While the disturbance amplitude is still higher in the shear layer than on the jet centerline, the rapid increase in disturbance amplitude is not observed in this case.

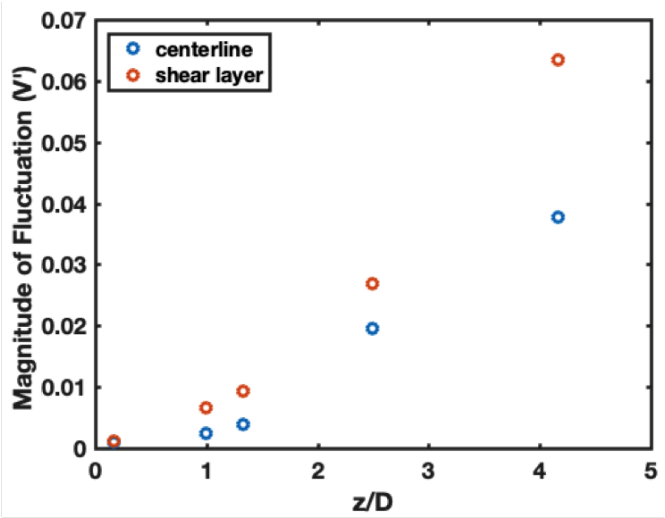

Figure 6.15: The amplitude of the disturbance is presented against the ve chosen axial locations. M=1, Re = 1682.

The spectral nature for each of these ten points is also investigated for observations of single-frequency peaks. Figure 6.16 shows FFTs for the ten points for a case when M = 26 and Re = 1682. A clear peak is seen in the plots, especially in the three middle locations.

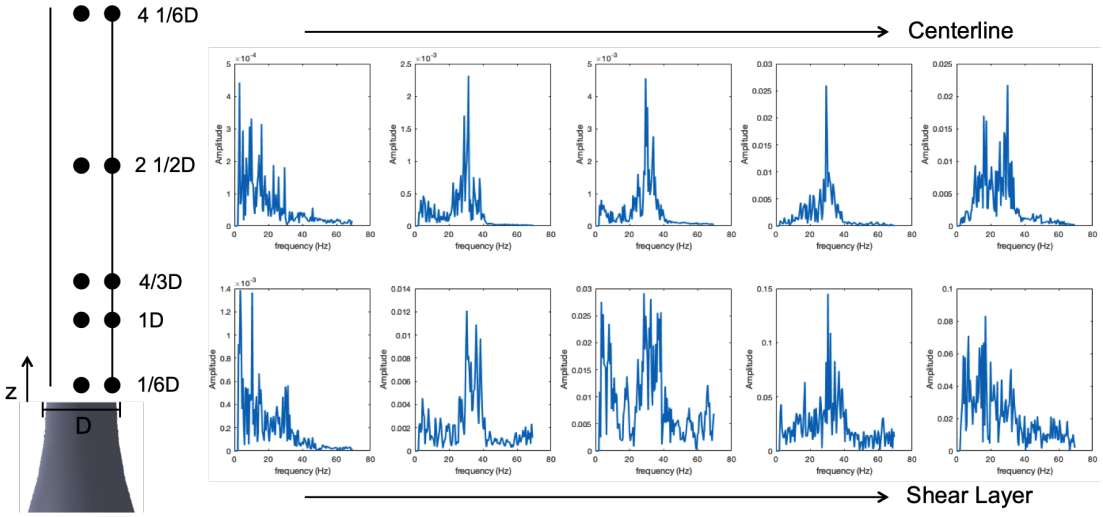

Figure 6.16: Schematic of the locations tested, and spectral data collected in those locations, M = 26, Re = 1682

The spectral nature of the jet in these same ten locations is also presented for a case with a lower Reynolds number of 841, as shown in Figure 6.17. It is readily apparent that the frequency of the most unstable mode is lower for this case.

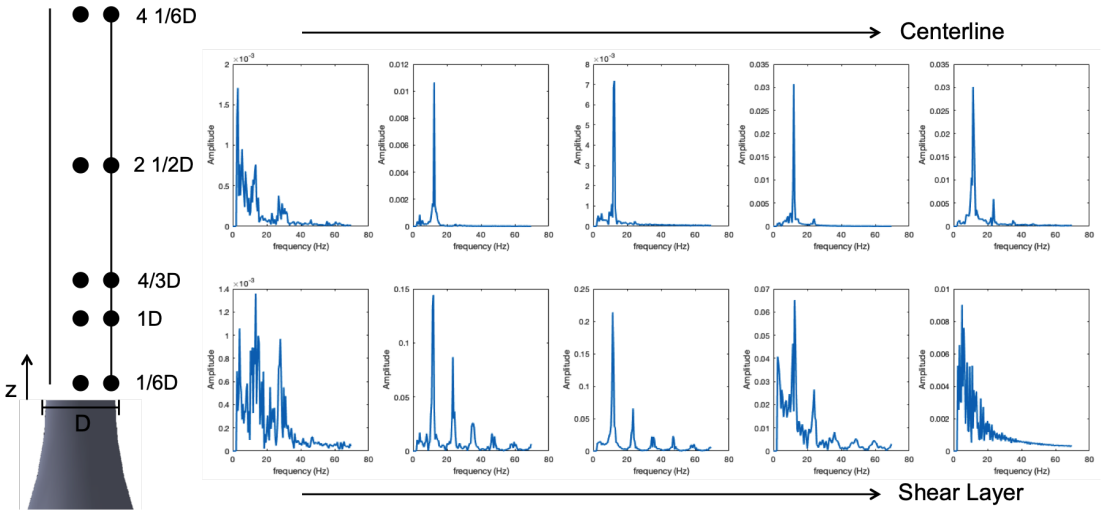

Figure 6.17: Schematic of the locations tested, and spectral data collected in those locations, M = 26, Re = 841

The jet disturbance frequencies are next examined systematically over the ten locations and the two Reynolds numbers (Re = 841, 1682) for six di erent viscosity ratios. These tests are the ones carried out - as stated in the methods section - by beginning with a tank of pure propylene glycol into which the saltwater jet issues. In between trials, the jet is turned on for a period of time until the overall tank viscosity reaches the next desired value. The tank is mixed, and a viscosity and speci c gravity measurement is taken at the new set point. This tank "viscosity dilution" is carried on until the six trials are completed. The trials are repeated twice and are done for both a slow (Re = 841) and fast (Re = 1682) case. The measured speci c gravities and viscosity ratios of these trials are shown in Figure 6.18.

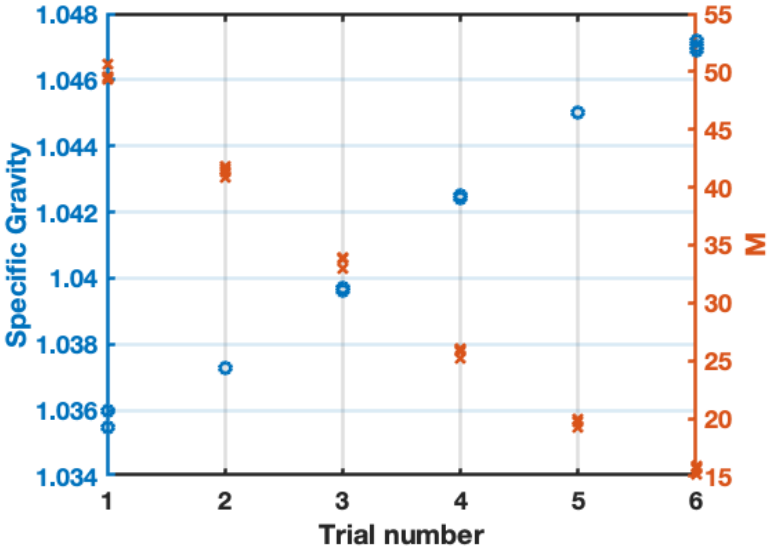

Figure 6.18: The speci c gravity and viscosity ratio values tested in the 10-point tests.

The most ampli ed frequency for each of the 10 positions is recorded at each viscosity ratio, for both of the two Reynolds number cases. The most ampli ed frequencies are then compared across locations and viscosity ratios. Plots of the most ampli ed frequencies, for both the centerline and shear layer locations are shown in Figure 6.19.

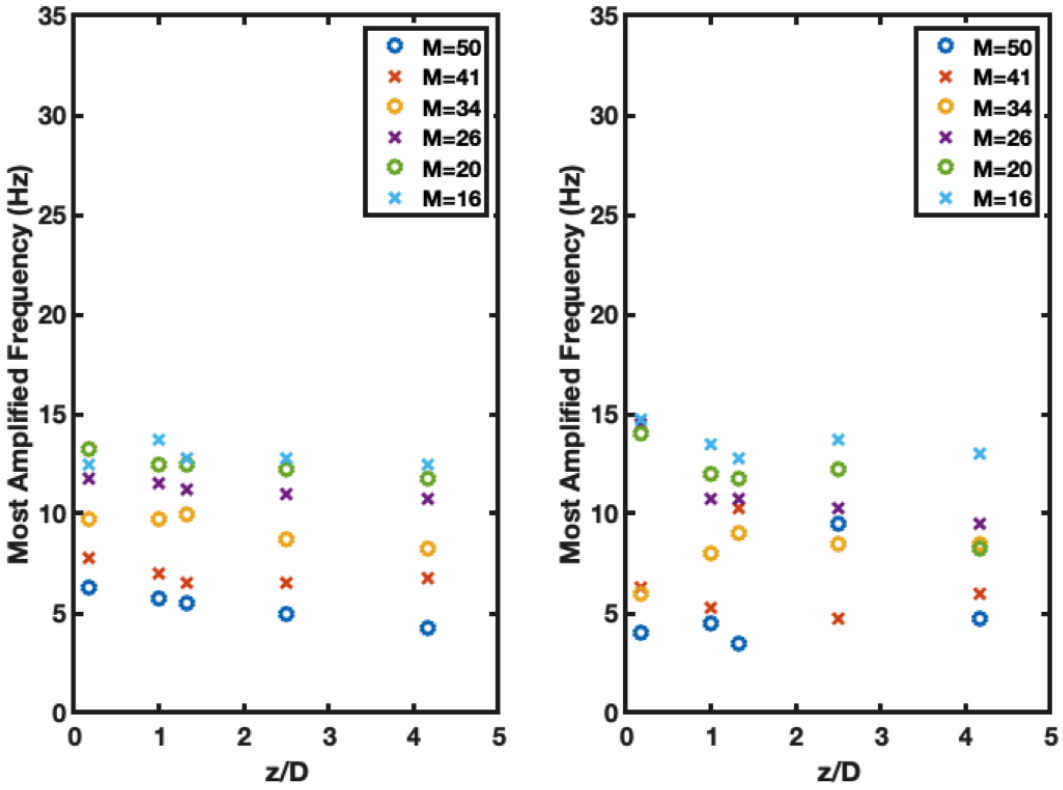

Figure 6.19: The most ampli ed frequencies are presented for the 6 viscosity ratio cases for ve centerline locations (left) and ve shear layer locations (right). Re = 841.

Note how the viscosity ratio appears to have an in uence on the most ampli ed frequency. While there is signi cant scatter in the data, the negative correlation between viscosity ratio and frequency is clearly seen. The data for the centerline is cleaner than the data in the shear layer. However, there is no clear di erence in most ampli ed frequency between the centerline and shear layer.

These results are presented as well for the Re = 1682 case in Figure 6.20. The data for this higher velocity case has much more scatter. However, the negative correlation between viscosity ratio and most ampli ed frequency is still observed. Overall, much higher frequencies are found in this higher Reynolds number case.

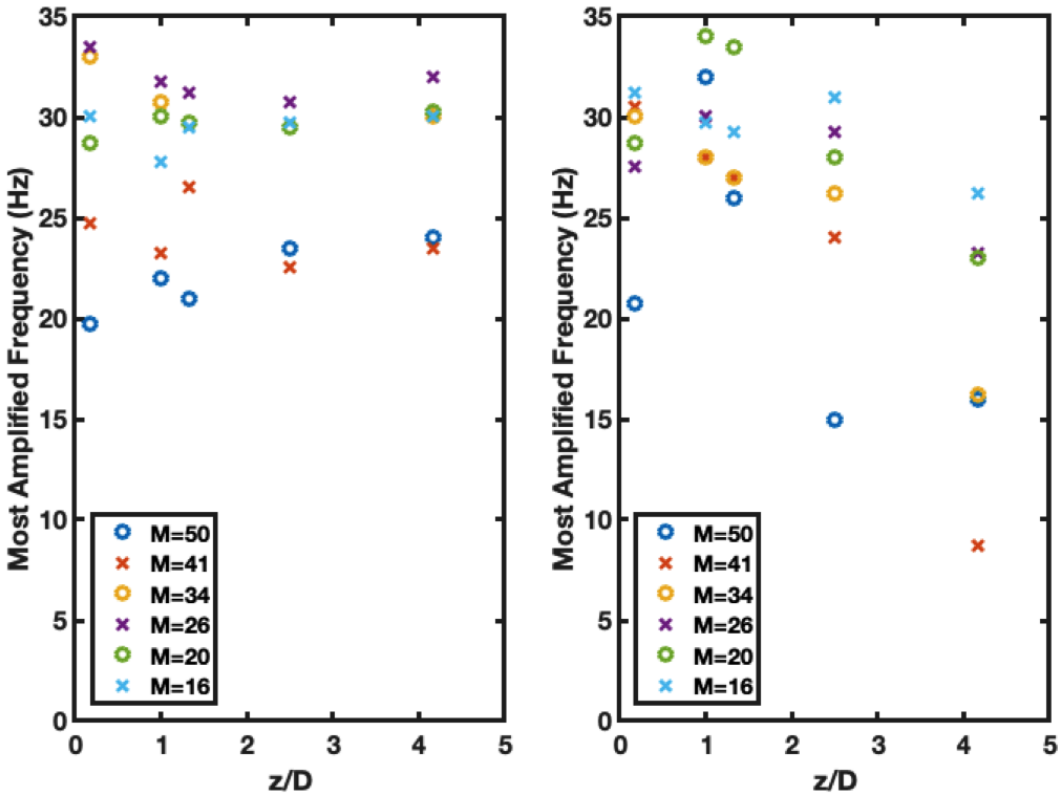

Figure 6.20: The most ampli ed frequencies are presented for the 6 viscosity ratio cases for ve centerline locations (left) and ve shear layer locations (right). Re = 1682.

Figure 6.21 compares the most ampli ed frequency with the viscosity ratio across trials. This plot uses the frequency data from a single location, by taking the frequency from the location with the most clearly de ned peak, as measured by the ratio of the peak amplitude to the next highest amplitude. The negative correlation between the viscosity ratio and most ampli ed frequency is clearly seen.

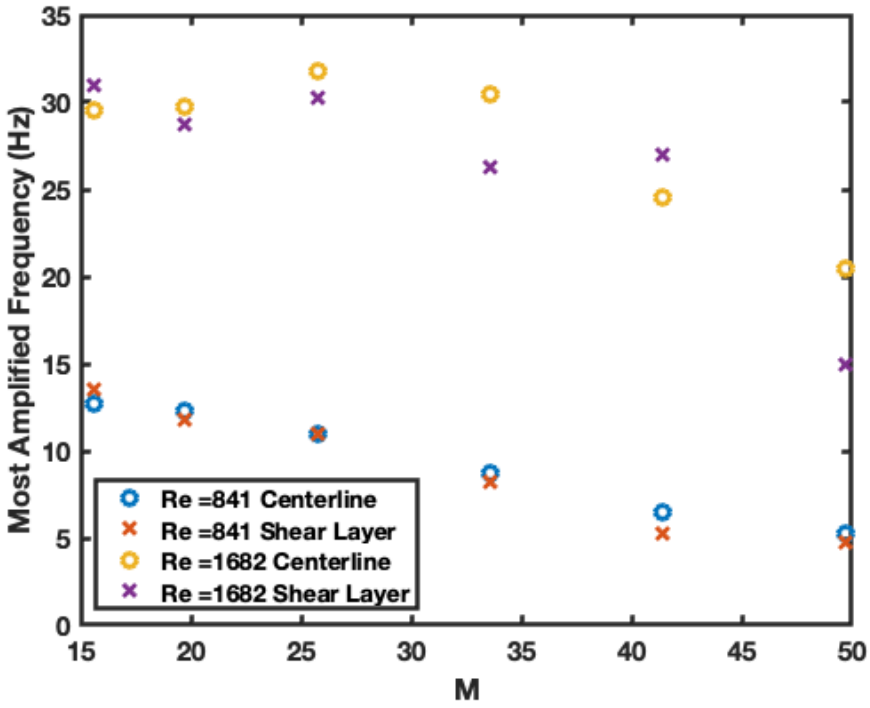

Figure 6.21: The most ampli ed frequencies are plotted against the 6 viscosity ratio cases for the Re = 841 and Re = 1682 cases, including both the centerline and shear layer measurements.

Overall, the jet is shown to have a frequency spectra with a de ned peak. The peak frequency is shown to have dependence on the jet Reynolds number and the viscosity ratio. However, a clear shift in the peak velocity across a certain viscosity ratio threshold is not observed, nor any other dramatic shift in behavior that is a clear marker of a global instability. More work will need to be done in order to determine whether such a shift in behavior indicative of a global mode may be captured in this facility as triggered by a viscosity ratio.

Chapter 7

Conclusions

An experimental facility was created to investigate the breakup of a round laminar jet with a jet-to-ambient viscosity ratio. The measurements taken in this facility have been documented. The key takeaways for this study are the following:

- The facility is successful in creating a laminar jet issuing into a quiescent media with matched density and variable viscosity. The chosen fluids of saltwater and propylene glycol allow for negligible density and surface tension effects, while creating ambient-to-jet viscosity ratios from M=1-50. The flowrate of the jet can be controlled to attain jet Reynolds numbers from Re = 400-2000. The jet is quiet and the is observed to contain very low levels of disturbance at the jet exit plane.
- The jet is observed to contain typical laminar jet characteristics of a turbulence intensity profile peaked in the boundary layer, a momentum thickness which scales with the square root of the Reynolds number, and a profile which can be described by a hyperbolic tangent.
- The technique of fluorescent dye imaging effectively visualizes the breakup of the jet. Both an axisymmetric and a helical breakup mode are observed. The mode of jet breakup appears to be dependent on both the jet Reynolds number and the jet-to-ambient viscosity ratio.
- The measurement technique of hot film anemometry effectively captures spectral aspects of the jet behavior. A narrow peak in the frequency spectrum is observed

for certain locations and jet conditions. The peak is not observed at the exit plane of the jet, becomes clearly observable above all other frequencies, and is lost among other frequencies at far downstream locations. The amplitude of the disturbance is higher in the shear layers, which is consistent with visualization observations of the axisymmetric and helical breakup modes.

- The most amplified frequency appears to be dependent on the jet Reynolds number and ambient-to-jet viscosity ratio. In this study, the most amplified frequency is negatively correlated with the ambient-to-jet viscosity ratio and positively correlated with the jet Reynolds number.

Future work should be carried out in order to further determine the existence of a global mode. One possible method is to perform forcing experiments, where a steady periodic frequency is applied to the test section, as discussed in Huerre and Monkewitz (1990). This forcing frequency is swept past suspected global-mode frequencies, and the corresponding "lock-in" of the jet is observed. Another method would be development of a counterflow nozzle, as discussed in Stykowski and Niccum (1991) so that higher shear levels can be achieved in the jet shear layer. Both of these methods could readily be implemented in the existing form of this experimental facility.

References

[Aul and Olbricht1990] Aul, R. and Olbricht, W. (1990). \Stability of a thin annular lm in pressure-driven, low-reynolds-number ow through a capillary." *Journal of Fluid Mechanics*, 215, 585{599.

[Berger1967] Berger, E. (1967). \Suppression of vortex shedding and turbulence behind oscillating cylinders." *The Physics of Fluids*, 10(9), S191{S193.

[Cao et al.2003] Cao, Q., Ventresca, A. L., Sreenivas, K., and Prasad, A. K. (2003). \Instability due to viscosity strati cation downstream of a centerline injector." *The Canadian Journal of Chemical Engineering*, 81(5), 913{922.

[Craik1969] Craik, A. D. (1969). \The stability of plane couette ow with viscosity strati cation." *Journal of Fluid Mechanics*, 36(4), 685{693.

[Drazin and Reid1981] Drazin, P. and Reid, W. (1981). *Hydrodynamic stability*.

[Drubka and Nagib1981] Drubka, R. E. and Nagib, H. M. (1981). \Instabilities in near eld of turbulent jets and their dependence on initial conditions and reynolds number." *Report no.*, ILLINOIS INST OF TECH CHICAGO DEPT OF MECHANICAL ENGINEERING.

[Govindarajan2004] Govindarajan, R. (2004). \E ect of miscibility on the linear instability of two- uid channel ow." *International Journal of Multiphase Flow*, 30(10), 1177{1192.

[Govindarajan and Sahu2014] Govindarajan, R. and Sahu, K. C. (2014). \Instabilities in viscosity-strati ed ow." *Annual review of uid mechanics*, 46, 331{353.

[Hallberg and Strykowski2006] Hallberg, M. and Strykowski, P. (2006). \On the universality of global modes in low-density axisymmetric jets." *Journal of Fluid Mechanics*, 569, 493{507.

[Hu and Joseph1989] Hu, H. H. and Joseph, D. D. (1989). \Lubricated pipelining: stability of core-annular ow. part 2." *Journal of uid mechanics*, 205, 359{396.

[Huerre and Monkewitz1990] Huerre, P. and Monkewitz, P. A. (1990). \Local and global instabilities in spatially developing ows." *Annual review of uid mechanics*, 22(1), 473{537.

[Jendoubi and Strykowski1994] Jendoubi, S. and Strykowski, P. (1994). \Absolute and convective instability of axisymmetric jets with external ow." *Physics of Fluids*, 6(9), 3000{3009.

[Kao and Park1972] Kao, T. W. and Park, C. (1972). \Experimental investigations of the stability of channel ows. part 2. two-layered co-current ow in a rectangular channel." *Journal of Fluid Mechanics*, 52(3), 401{423.

[Kouris and Tsamopoulos2001] Kouris, C. and Tsamopoulos, J. (2001). \Dynamics of axisymmetric core-annular ow in a straight tube. i. the more viscous uid in the core, bamboo waves." *Physics of Fluids*, 13(4), 841{858.

[Kundu et al.2015] Kundu, P. K., Dowling, D. R., Tryggvason, G., and Cohen, I. M. (2015). \Fluid mechanics.

[Kyle1988] Kyle, D. (1988). \Lif images of he/n2 jets." *Dept. Mech. Engng Rep. FM88DK1. Yale University*.

[Kyle and Sreenivasan1993] Kyle, D. and Sreenivasan, K. (1993). \The instability and breakdown of a round variable-density jet." *Journal of Fluid Mechanics*, 249, 619{664.

[Landau et al.2013] Landau, L. D., Bell, J., Kearsley, M., Pitaevskii, L., Lifshitz, E., and Sykes, J. (2013). *Electrodynamics of continuous media*, Vol. 8. elsevier.

[Lecordier et al.1991] Lecordier, J.-C., Hamma, L., and Paranthoen, P. (1991). \The control of vortex shedding behind heated circular cylinders at low reynolds numbers." *Experiments in Fluids*, 10(4), 224{229.

[Lin1946] Lin, C. (1946). \On the stability of two-dimensional parallel ows: Part iii.stability in a viscous uid." *Quarterly of Applied Mathematics*, 3(4), 277{301.

[Mathis et al.1984] Mathis, C., Provansal, M., and Boyer, L. (1984). \The bernard-von karman instability: an experimental study near the threshold." *Journal de Physique Lettres*, 45(10), 483{491.

[Monkewitz1988] Monkewitz, P. A. (1988). \The absolute and convective nature of instability in two-dimensional wakes at low reynolds numbers." *The Physics of uids*, 31(5), 999{1006.

[Monkewitz et al.1990] Monkewitz, P. A., Bechert, D. W., Barsikow, B., and Lehmann, B. (1990). \Self-excited oscillations and mixing in a heated round jet." *Journal of Fluid Mechanics*, 213, 611{639.

[Niccum1990] Niccum, D. (1990). \The in uence of velocity ratio on a counter owing circular jet." M.S. thesis, University of Minnesota, University of Minnesota.

[Noto et al.1985] Noto, K., Ishida, H., and Matsumoto, R. (1985). \A breakdown of the karman vortex street due to the natural convection." *Flow Visualization*, 3, 348{354.

[Ranganathan and Govindarajan2001] Ranganathan, B. T. and Govindarajan, R. (2001). \Stabilization and destabilization of channel ow by location of viscosity-strati ed uid layer." *Physics of Fluids*, 13(1), 1{3.

[Sahu and Matar2010] Sahu, K. C. and Matar, O. (2010). \Three-dimensional linear instability in pressure-driven two-layer channel ow of a newtonian and a herschel{ bulkley uid." *Physics of Fluids*, 22(11), 112103.

[Schmid and Henningson2000] Schmid, P. and Henningson, D. (2000). *Stability and Transition in Shear Flows*. Applied Mathematical Sciences. Springer New York, <https://books.google.com/books?id=5eNoy2VdXo8C>.

[Selvam et al.2007] Selvam, B., Merk, S., Govindarajan, R., and Meiburg, E. (2007). \Stability of miscible core{annular ows with viscosity strati cation." *Journal of Fluid Mechanics*, 592, 23{49.

[Sreenivasan et al.1989] Sreenivasan, K., Raghu, S., and Kyle, D. (1989). \Absolute instability in variable density round jets." *Experiments in Fluids*, 7(5), 309{317.

[Sreenivasan et al.1987] Sreenivasan, K., Strykowski, P., and Olinger, D. (1987). \Hopf bifurcation, landau equation, and vortex shedding behind circular cylinders." *Forum on unsteady ow separation*, Vol. 1, ASME New York, 1{13.

[Srinivasan et al.2010] Srinivasan, V., Hallberg, M., and Strykowski, P. J. (2010). \Viscous linear stability of axisymmetric low-density jets: parameters in uencing absolute instability." *Physics of Fluids*, 22(2), 024103.

[Strykowski and Niccum1991] Strykowski, P. and Niccum, D. (1991). \The stability of countercurrent mixing layers in circular jets." *Journal of Fluid Mechanics*, 227, 309{343.

[Strykowski and Sreenivasan1990] Strykowski, P. and Sreenivasan, K. (1990). \On the formation and suppression of vortex sheddingat low reynolds numbers." *Journal of Fluid Mechanics*, 218, 71{107.

[Strykowski1986] Strykowski, P. J. (1986). \The control of absolutely and convectively unstable shear ows." Ph.D. thesis, Yale University, Yale University.

[Todde et al.2009] Todde, V., Spazzini, P. G., and Sandberg, M. (2009). \Experimental analysis of low-reynolds number free jets." *Experiments in uids*, 47(2), 279{294.

[Twiss1951] Twiss, R. (1951). \On oscillations in electron streams." *Proceedings of the Physical Society. Section B*, 64(8), 654.

[Woods1969] Woods, J. (1969). \On richardson's number as a criterion for laminar-turbulent-laminar transition in the ocean and atmosphere." *Radio Science*, 4(12), 1289{1298.

[Yasuo et al.1986] Yasuo, M., Kunio, H., and Takayoshi, N. (1986). \A fundamental study of symmetrical vortex generation behind a cylinder by wake heating or by splitter plate or mesh." *International journal of heat and mass transfer*, 29(8), 1193{1201.

[Yih1967] Yih, C.-S. (1967). \Instability due to viscosity strati cation." *Journal of Fluid Mechanics*, 27(2), 337{352.

[Monkewitz et al.1990] [Strykowski and Niccum1991] [Govindarajan and Sahu2014]
[Jendoubi and Strykowski1994] [Kyle and Sreenivasan1993] [Srinivasan et al.2010]
[Schmid and Henningson2000] [Huerre and Monkewitz1990] [Drazin and Reid1981]
[Woods1969] [Kundu et al.2015] [Twiss1951]
[Landau et al.2013] [Sahu and Matar2010] [Lin1946]
[Craik1969] [Govindarajan2004] [Hu and Joseph1989]
[Yih1967] [Kao and Park1972] [Aul and Olbricht1990]
[Kouris and Tsamopoulos2001] [Ranganathan and Govindarajan2001] [Selvam et al.2007]
[Cao et al.2003] [Mathis et al.1984] [Strykowski1986]
[Noto et al.1985] [Yasuo et al.1986] [Strykowski and Sreenivasan1990]
[Lecordier et al.1991] [Berger1967] [Monkewitz1988]
[Kyle1988] [Sreenivasan et al.1987] [Hallberg and Strykowski2006]
[Sreenivasan et al.1989] [Todde et al.2009] [Drubka and Nagib1981]
[Niccum1990]

Appendix A

Hotfilm Calibration Technique

First, the jet is run for 7 different flowrates and the resulting anemometer voltages are recorded. An example plot of this is shown in Figure A.1.

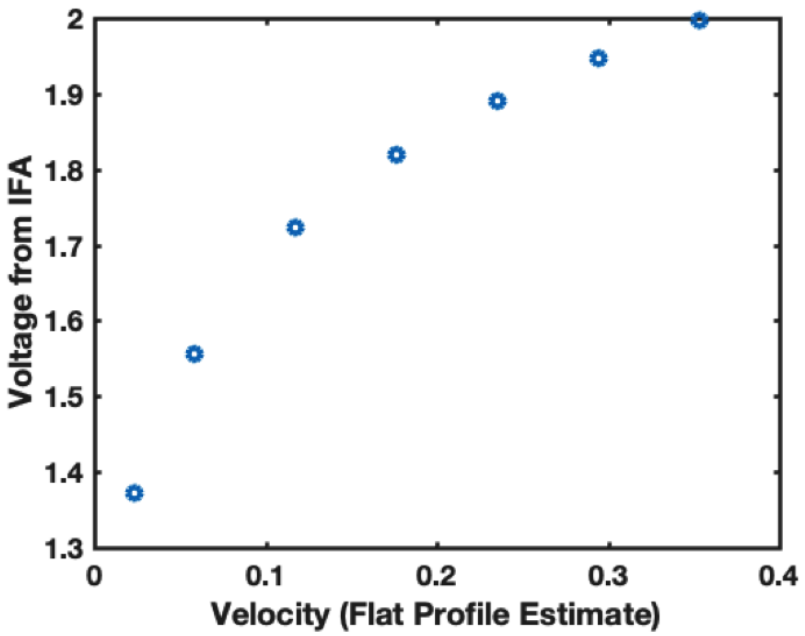

Figure A.1: Example calibration curve for the hot film probe

The velocity values on the x-axis of Figure A.1 are calculated using the measured flowrate from the flowmeter and the diameter of the jet. Using this velocity estimate, a

linearized calibration curve is generated using the generalized Kings Law:

$$E^2 = A + BU^{1/n} \tag{A.1}$$

In Equation A.1, E is the voltage from the anemometer, U is the ow velocity, and A, B, and n are coe cients t to best linearize the data. The linear t is shown on top of the data points in Figure A.2.

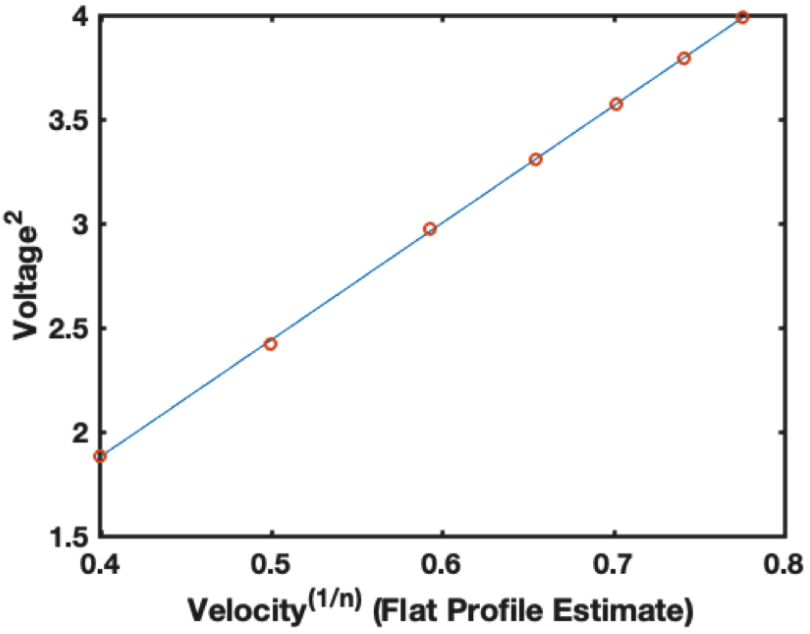

Figure A.2: Example of a calibration t using King's law

This t assumes a perfect tophat pro le coming from the nozzle. However, the true pro le includes a boundary layer of decreased velocity, as shown in Figure A.3.

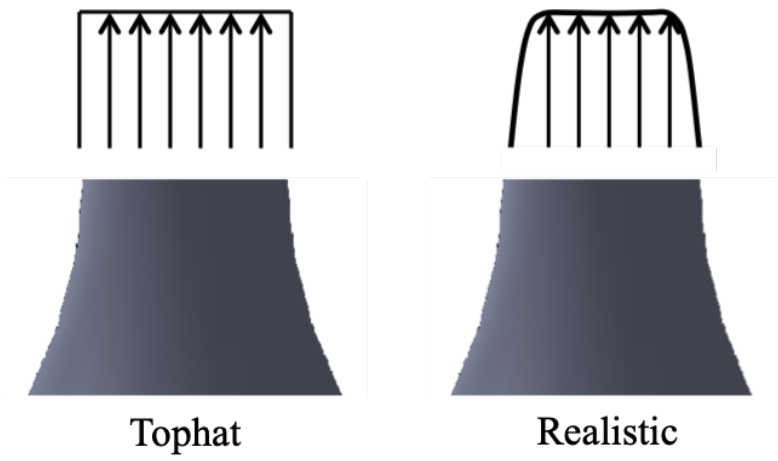

Figure A.3: Schematic of tophat and realistic jet pro les.

As a way to decrease error, the calibration is augmented using a volume-matching technique. First, high- delity radial jet pro les are taken at 0.5mm from the jet exit plane for each calibration owrate. The calibration t is then applied to each of these pro les to convert the voltages to velocities, as shown in Figure A.4.

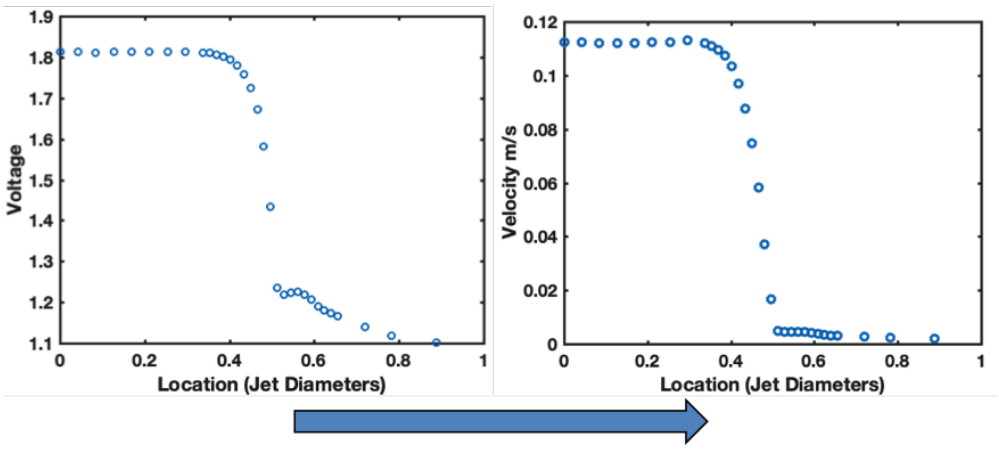

Figure A.4: Example of a jet pro le being converted from voltages (left) to velocities (right) using the calibration curve.

The owrate through the nozzle exit, given the current jet pro le, can be found by spinning the jet pro le around the jet centerline. This spun volume is then compared to the volume of an ideal tophat jet. This is done for each of the seven owrate pro les.

As seen in the Figure A.5, the jet pro le volumes initially do not match up with the true volumes.

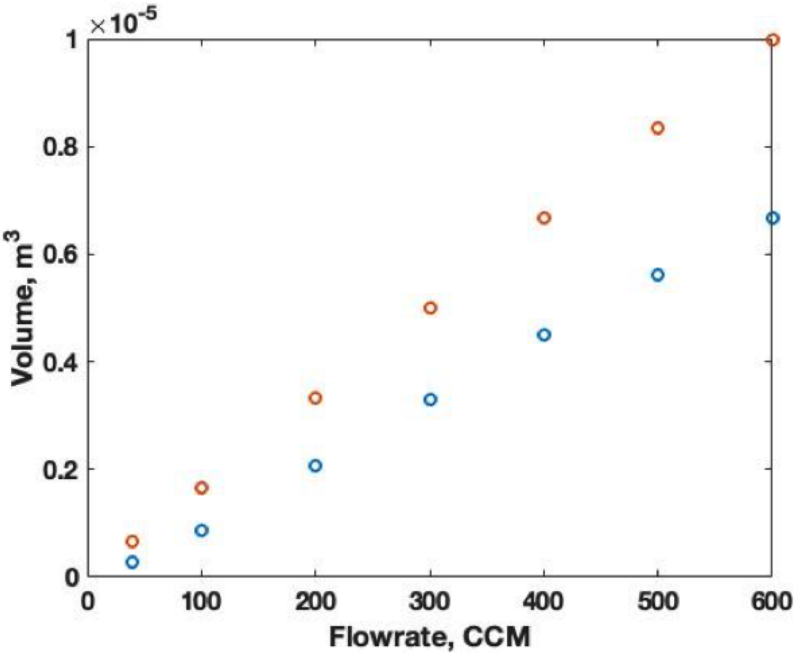

Figure A.5: Plot of volumes calculated for ideal tophat pro le jets (orange) and calculated from measured jet pro les (blue).

In order to make the two volumes match, the coe cient B is tweaked in King's Law Equation A.1. This is the equivalent of stretching or compressing the pro les. Figure A.6 shows how the volumes match well when B is multiplied by 0.905:

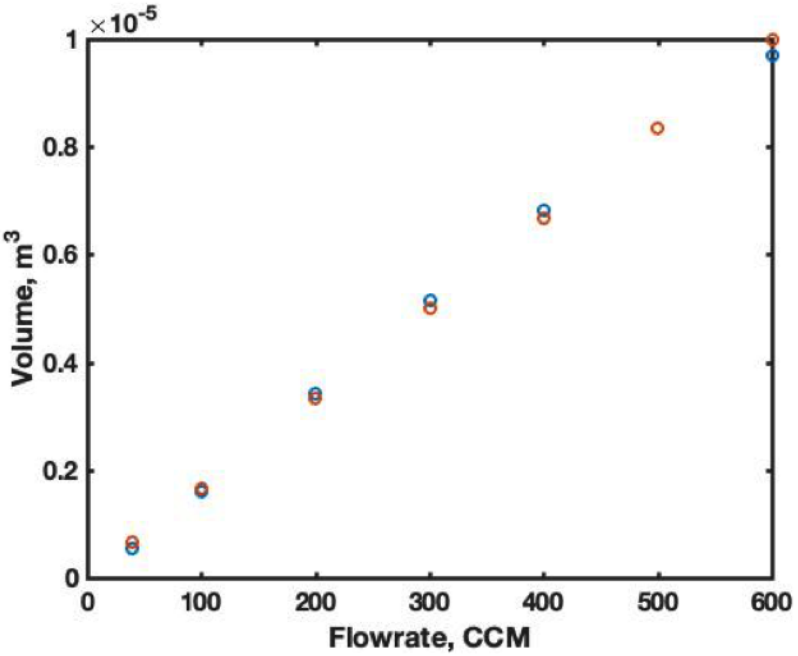

Figure A.6: Plot of volumes calculated for ideal tophat pro le jets (orange) and calculated from measured jet pro les (blue) after applying an adjustment to King's law coe cient B.

The King's law calibration with the new value of coe cient B is now used for subsequent voltage to velocity conversions.

Appendix B

Error Analysis

The total uncertainty in the velocity measurements is a result of uncertainty from the voltage measurement by the multimeter, the uncertainty of the calibration regression, and the systematic uncertainty from the owrate measured through the owmeter.

$$U = \sqrt{U_{flowmeter}^2 + U_{voltage}^2 + U_{regression}^2} \tag{B.1}$$

The uncertainty of the owmeter is 3%, which corresponds to a owrate uncertainty of 5 ccm. This, converted to the base, average velocity value used in the calibration, corresponds to a velocity uncertainty of 0.009 m/s.

To nd the uncertainty in the regression t, we rst nd the uncertainty of E^2, and propagate it through to nd the corresponding $U_{regression}^2$:

$$U = \frac{dU}{dE^2} \quad E^2 = \frac{1}{n}\frac{E^2}{B^2} \quad A^{\frac{1}{n}} \quad ^1 \tag{B.2}$$

For the worst case (highest) velocity trials, this comes out to a value of 4.22E-4 m/s,

The multimeter used (Agilent 34411A) has an uncertainty of 0.003% of reading and 0.0005% of range. Each velocity point corresponds to a minimum of 1024 measurements taken. The uncertainty from the multimeter is therefore taken to be 6.32E-4 V.

The total velocity uncertainty is therefore calculated to be:

$$U = 0.01 m/s \tag{B.3}$$

which comes primarily from the uncertainty in the owmeter. This uncertainty corresponds to an uncertainty range of 3.5-10% of reading over the Reynolds number range presented.

The frequency resolution for the FFt is Fs/N, where Fs is the sample frequency and N is the number of sample points used in the FFt. For the worst case sample trials of 1024 data points in 1 second, the corresponding frequency resolution is 1 Hz. For the frequency results presented, where a sampling frequency of 1024 Hz was used for 2 seconds, the resolution is 0.5 Hz. As for the error in the magnitude of the disturbance at the peak frequency, the plots and analysis presented are treated qualitatively, and no arguments are based on the statistical analysis of the magnitudes. For this reason, no uncertainty values are computed in this case.